Multi-approach study of nose landing gear noise

Merino-Martínez, Roberto; Neri, Eleonora; Snellen, Mirjam; Kennedy, John; Simons, Dick G.; Bennett, Gareth J.

DOI
10.2514/1.C035655

Publication date
2020

Document Version
Accepted author manuscript

Published in
Journal of Aircraft

Citation (APA)
Merino-Martínez, R., Neri, E., Snellen, M., Kennedy, J., Simons, D. G., & Bennett, G. J. (2020). Multi-approach study of nose landing gear noise. *Journal of Aircraft*, *57*(3), 517-533. https://doi.org/10.2514/1.C035655

A multi–approach study of nose landing gear noise

Roberto Merino-Martínez[a]
Delft University of Technology, 2629 HS Delft, the Netherlands

Eleonora Neri[b]
Trinity College Dublin, Ireland and B–Fluid Ltd. Dublin, Ireland

Mirjam Snellen[c]
Delft University of Technology, 2629 HS Delft, the Netherlands

John Kennedy[d]
Trinity College Dublin, Ireland

Dick G. Simons[e]
Delft University of Technology, 2629 HS Delft, the Netherlands

Gareth J. Bennett[f]
Trinity College Dublin, Ireland

The noise emissions of a full–scale nose landing gear (NLG), measured in a wind tunnel and obtained from computational simulations, are compared with those of three regional aircraft types recorded in flyover measurements. A comparison is made with the noise prediction models of Fink, Guo, and DLR. A good agreement was found between all the spectra. The noise emissions up to 1.2 kHz were found to scale with the 6^{th} power of the flow velocity, as usual; however, the spectra at higher frequencies collapsed better when scaled to the 7^{th} power, confirming the fact that high-frequency noise is radiated from the turbulent flow surrounding small features of the NLG. Microphone

[a] PhD, Postdoctoral researcher, Aircraft Noise & Climate Effects section, Faculty of Aerospace Engineering, Kluyverweg 1. AIAA member. E-mail: r.merinomartinez@tudelft.nl

[b] Aerodynamics engineer, PhD, Department of Mechanical and Manufacturing Engineering. E-mail: eneri@tcd.ie

[c] Associate professor, Aircraft Noise & Climate Effects section, Faculty of Aerospace Engineering, Kluyverweg 1. E-mail: m.snellen@tudelft.nl

[d] Assistant Professor, Department of Mechanical and Manufacturing Engineering. E-mail: kennedj@tcd.ie

[e] Full professor, Aircraft Noise & Climate Effects section, Faculty of Aerospace Engineering, Kluyverweg 1. E-mail: d.g.simons@tudelft.nl

[f] Associate Professor, Department of Mechanical and Manufacturing Engineering. AIAA Senior Member. E-mail: gareth.bennett@tcd.ie

arrays showed that the main noise sources were located in the middle of the wheel axle. For the flyovers and computational simulations, strong tonal peaks (at around 2200 Hz) were found, which are likely to be caused by open cavities in the NLG. This phenomenon is not accounted for in prediction models. Removing these tones would result in noise reductions of up to 2 dB. Thus, it is highly recommended to include cavity–noise estimations in the current prediction models, or to simply eliminate such cavities where possible with the use of cavity caps.

Nomenclature

Latin symbols

$\hat{A}$	=	Empirical parameter for Guo's method
$\hat{b}$	=	Empirical parameter for Guo's method
$\hat{B}$	=	Empirical parameter for Guo's method
c	=	Speed of sound
d	=	Diameter
$\hat{D}$	=	Directivity function
f	=	Sound frequency
$\hat{F}$	=	Spectrum function
$\hat{h}$	=	Empirical parameter for Guo's method
K_1	=	Empirical parameter for Fink's method
K_2	=	Empirical parameter for Fink's method
l	=	Characteristic length
L_p	=	Sound Pressure Level
$L_\mathrm{p,A}$	=	A–weighted sound pressure level
M	=	Mach number
N_strut	=	Number of struts in a landing gear
N_wheel	=	Number of wheels in a landing gear
p	=	Static acoustic pressure
P	=	Acoustic power

$\hat{q}$ = Empirical parameter for Guo's method

r = Distance between the sound source and the observer

S = Reference surface area

St = Strouhal number

V = Flow velocity

w = Width

(x, y, z) = Cartesian coordinates

Greek symbols

α = Atmospheric absorption coefficient

$\hat{\beta}$ = Flow energy conversion efficiency parameter for Guo's method

Δf = Frequency resolution

$\hat{\eta}$ = Complexity factor for Guo's method

$\hat{\mu}$ = Empirical parameter for Guo's method

ν = Functional beamforming exponent

θ = Polar sound emission angle

ρ = Air density

$\hat{\sigma}$ = Empirical parameter for Guo's method

ϕ = Azimuthal sideline emission angle

Subscripts

cavity = Referring to the cavity

high = High–frequency

k = k^{th} sound source

low = Low–frequency

mid = Mid–frequency

ref = Reference

strut = Referring to the strut of a landing gear

wheel = Referring to the wheel of the landing gear

Acronyms

ACARE = Advisory Council for Aviation Research and Innovation in Europe

ADS–B = Automatic Dependent Surveillance–Broadcast

ALLEGRA = Advanced Low noise Landing (main and nose) Gear for Regional Aircraft

ANOPP = Aircraft NOise Prediction Program

CFDBF	=	Conventional Frequency Domain BeamForming
CSM	=	Cross–Spectral Matrix
DAMAS	=	Deconvolution Approach for the Mapping of Acoustic Sources
DNB	=	Direct Numerical Beamforming
DLR	=	Deutsches Zentrum für Luft- und Raumfahrt e.V. (German Aerospace Center)
FAA	=	Federal Aviation Administration
FW–H	=	Ffowcs Williams–Hawkings
GRA	=	Green Regional Aircraft
IDDES	=	Improved Delayed Detached Eddy Simulation
KTH	=	Kungliga Tekniska Högskolan (Royal Institute of Technology, Sweden)
LAGooN	=	LAnding Gear nOise database and CAA validatiON
LG	=	Landing gear
LPD	=	Linear Programming Deconvolution
MLG	=	Main Landing Gear
NASA	=	National Aeronautics and Space Administration
NLG	=	Nose Landing Gear
ONERA	=	Office National d'Études et de Recherches Aérospatiales (French Aerospace Lab)
PANAM	=	Parametric Aircraft Noise Analysis Modul
PSF	=	Point Spread Function
ROI	=	Region Of Integration
SME	=	Small and Medium–sized Enterprise
SPA	=	Pininfarina Società Per Azioni (SPA)
SPI	=	Source Power Integration
SPL	=	Sound Pressure Level

I. Introduction

The noise impact from aircraft is becoming an increasingly important issue for the aerospace industry because it causes severe annoyance for the population living around airports. Environmental noise is currently considered the second biggest health threat in Europe after air pollution [1]. Technological advances over the last decades, such as high–bypass turbofan engines and acoustic liners [2], have achieved considerable reductions in the engine noise levels. Thus, airframe noise

(generated by the interaction between the aerodynamic surfaces and the surrounding unsteady turbulent flow [3]) can present comparable sound pressure levels (SPL or L_{p}) as engine noise during the approach stage because the engines normally operate at low thrust settings, and it may constitute a lower bound to aircraft noise in the future [4, 5]. Governmental organizations, such as ACARE [6] (Advisory Council for Aviation Research and Innovation in Europe) and projects such as Flight Path 2050 [7] aim for a 65% reduction of the perceived aircraft noise levels by 2050 compared to the levels in 2000 (equivalent to a reduction of 15 dB per operation).

Within this framework, the European Clean Sky–funded project ALLEGRA (Advanced Low Noise Landing (Main and Nose) Gear for Regional Aircraft) was developed to assess the performance of low–noise technologies applied to a full–scale nose landing gear (NLG) model [8, 9] and a half–scale main landing gear (MLG) model [10] of a high–wing, environmentally–aware regional aircraft. This aircraft design belongs to the Green Regional Aircraft (GRA) project, which is a Clean Sky 1 integrated technology demonstrator [11]. ALLEGRA consisted of a consortium of universities (Trinity College Dublin and Kungliga Tekniska Högskolan (KTH)), an aeroacoustic wind–tunnel company (Pininfarina Società Per Azioni (SPA)), and European small and medium–sized Enterprises (SME) manufacturing and design partners (Eurotech and Teknosud) supported by a leading landing gear manufacturer (Magnaghi Aeronautica).

The main source of airframe noise for modern commercial aircraft is the landing gear (LG) system [5, 12]. The LG system typically consists of complicated structures of bluff bodies (struts, links, wheels, tires, fairings, etc.) of considerably different sizes, which are normally not optimized acoustically [4]. The sound generation mechanisms for LG systems are usually very complex and depend on the specific geometry and configuration of the LG. A typical sound signal from a LG system is a combination of broadband noise, mainly caused by the interaction of the LG with turbulent flow, and tonal noise, generated by cavity resonances [4, 13, 14] and Aeolian tones due to flow separation and vortex shedding [15, 16]. The tonal frequency due to a cavity mainly depends on the cavity geometry itself [13], where specific tones corresponding to a range of resonant duct modes can be excited depending on the velocity range of the aircraft [17–19]. The frequency of the Aeolian tones, however, changes as the flow velocity varies [16]. The contribution of the Aeolian tones to the

overall noise levels is typically negligible and their tonal frequencies are usually considerably lower (around 100 Hz) than those corresponding to cavity noise.

The noise emissions of the whole LG system are due to the combination of the contributions of the NLG and the MLG systems. Even though the MLG structure is typically larger and more complicated than the NLG (i.e., it is expected to be noisier), the flow velocity impinging the MLG system is approximately 20% lower than that of the NLG because of the recirculation of the flow underneath the wings where the MLG is usually located [20, 21]. Therefore, due to the strong dependence between the LG noise levels and the flow velocity [22], this difference in velocity causes a decrease of about 6 dB and, consequently, both LG systems often emit comparable noise levels [23]. The object of study of this paper is the NLG system of regional aircraft (within the context of the ALLEGRA project). Despite being smaller and typically quieter than wide–body, long–range aircraft, regional aircraft represent a considerable share of the total flights in Europe (about 30% of the flights recorded in the measurement campaigns performed in [24, 25]).

There are several approaches to study LG noise. The methods employed in this paper are briefly described below, as well as their benefits and limitations:

1. **Wind–tunnel measurements** [8–10, 15, 26] offer relatively controlled flow conditions, but they require the LG model being tested to have a high level of geometric detail to represent the small–scale sound generating mechanisms [5, 12]. Moreover, it is difficult to replicate the exact conditions present around a flying aircraft, such as the Reynolds number or installation effects [27]. This approach also lacks the important feature of the relative motion between source and receiver [4]. According to Dobrzynski [5], noise prediction models based solely on wind–tunnel tests featuring scale models are prone to underestimate airframe noise levels compared to full–scale flight tests , mainly because simplified wind–tunnel models do not capture all the geometric details. A detailed representation is especially essential for cavity noise, which can be a dominant noise source, like in the case of the Airbus A320 fuel overpressure vents [5]. In this paper, wind tunnel measurements [24, 28] of the full–scale, high fidelity NLG model within the ALLEGRA project are considered. The model includes the wheel bay, doors, fairings and a large portion of the nose fuselage all of which set the campaign apart compared to previous

tests.

2. **Flyover measurements** [12, 23, 24, 29] with aircraft under operational conditions present different challenges, such as the inability to control the aircraft position, larger distances between the sound source and the observer, and less–controlled aerodynamic and atmospheric characteristics, but they fully represent the actual conditions experienced in reality [30–32], such as crosswind. Hence, a comparison between the results of flyover measurements to wind–tunnel experiments is of great interest [16]. Flyover field measurements under operational conditions recorded at Amsterdam Airport Schiphol [24] are employed in this study. Three different regional aircraft types (all equipped with turbofan engines) are selected for this paper.

3. **Computational simulations** [33–35] of a detailed LG geometry can be very time–consuming due to its complex structure. On the other hand, extensive wind–tunnel or flyover test campaigns usually have a large economic cost, limiting the amount of configurations available for study. In practice, for numerical simulations, the geometry of the LG is normally simplified to some extent such that the computational cost is acceptable. This is also the case for the realistic NLG geometry from the ALLEGRA project [33–35] or the more simplified LAGooN geometry from ONERA [36]. The main advantages of computational simulations are that they offer insight into the noise generation mechanisms since they provide the flow characteristics, they allow for non–intrusive measurements in directions that are practically impossible to investigate in experiments (such as upwind of the model) and that the acoustic data are usually *cleaner* than those recorded in experiments since there is virtually no background noise. For this research, the computational simulations on the ALLEGRA NLG geometry performed by Bouchouireb *et al.* [33] are used for comparison.

4. **Noise prediction models** relying on empirical data or semi–empirical estimations provide one–third–octave–band noise spectra estimations for different directivity angles for simplified LG geometries. They require some geometrical parameters as input, but they normally do not consider parasitic noise sources, such as cavities [23, 24]. Previous studies [23, 37–40] showed that considerable differences exist between experimental measurements and the model

predictions for LG noise. In addition, by their very nature, semi–empirical methods have a limited reliability in predicting the impact of noise reduction devices [33]. The noise prediction methods of Fink [22], Guo [37, 41], and the German Aerospace Center (DLR) [21] are applied to the ALLEGRA NLG geometry.

For aeroacoustic measurements, it is common to employ phased microphone arrays and acoustic imaging techniques for estimating the location and strength of the sound sources [9, 42–47] and isolate their contributions. The application of acoustic imaging to simulated data is, however, relatively new, yet promising and in intense development [33, 48].

For this research, both sets of experimental measurements and the computational simulations employ phased microphone arrays (a virtual array in the computational case) to separate the sound signals emitted by the NLG. The performance of the three noise prediction models (Fink's, Guo's, and DLR's methods) will be compared to the experimental and numerical results.

The paper is structured as follows: Section II explains the experimental setups for the wind–tunnel and flyover measurements and the numerical setup and computational domain for the simulated case. Details about the NLG geometries considered are also included. The acoustic imaging techniques employed are summarized in Sec. III. Brief descriptions of Fink's and Guo's, and DLR's noise prediction models are provided in Sec. IV. The results obtained and the comparison between approaches are presented in Sec. V and Sec. VI gathers the most important conclusions.

II. Experimental and numerical setups

A. Wind–tunnel measurements

The NLG model used in the ALLEGRA project was full–scale, including a full representation of the NLG details and associated structures (e.g., bay cavity, bay doors, nose fuselage and hydraulic dressings). The LG geometry was obtained from an advanced regional turboprop aircraft design.

The experiments were performed in the Pininfarina open–jet, semi–cylindrical wind–tunnel facility in Turin, Italy, which has a test section of 8 m (length) $\times$ 9.60 m (width) $\times$ 4.20 m (height). The facility contains a low–noise, high–speed fan–driven system of 13 fans, which provides flow velocities up to 72.2 m/s and presents a background noise level of 68 dBA at 27.8 m/s. The

background noise for the ALLEGRA NLG tests was a combination of the wind–tunnel noise and the noise produced by the fuselage itself. Both are mostly low frequency noise sources (below 100 Hz), outside of the frequency range of interest. The flow velocity produced by the wind tunnel is very uniform, since it varies by only 0.5% over the test area. The turbulence intensity level had a value of approximately 0.3% in these experiments.

Figure 1 depicts the relative position of the NLG model in the wind tunnel, as well as the coordinate system employed, where the xz plane is the symmetry plane of the test model, the yz plane corresponds to the wind–tunnel nozzle exit and the origin is situated on the floor of the testing platform (xy plane). The NLG complete model, with the fuselage belly, was placed in the wind tunnel so that the distance between the exit of the wind–tunnel's nozzle and the NLG wheel axis was 2.8 m. The coordinates of the middle point of the wheel axis were:

$$x = 2.8 \text{ m}; \; y = 0 \text{ m}; \; z = 2.175 \text{ m}.$$

Figure 2 shows a picture of the model inside the wind tunnel and Fig. 3 presents the overall dimensions of the wind–tunnel test model.

The wind–tunnel model had a fixed, built–in angle of attack of 4°. Each model configuration was tested at a variety of flow speeds and yaw settings, allowing the analysis of conditions equivalent to landing with crosswind. For this paper, only the yaw angle of 0° (no crosswind) was considered. Flow velocities of 40, 50, 60 and 65 m/s were employed for the experiment providing a maximum Mach number of about 0.19.

Four different planar microphone arrays were installed in the top, side and front of the wind tunnel outside of the flow. For the present study, only the data from two arrays were used:

1. For considering the acoustic emissions radiated in the *flyover* direction (i.e., for polar emission angles $\theta \approx 90°$) the top array was employed (illustrated in Fig. 4a). The array consisted of 78 microphones in a multi–arm spiral arrangement of approximately 3 m diameter. This array was located in the $z = 4$ m plane, i.e., at a distance to the NLG axis of 1.825 m.

2. To study the lateral or *side* emission pattern of the NLG (i.e., for azimuthal angles $\phi \approx 90°$) the side array was used (see Fig. 4b). The array was positioned in the $y = -4.22$ m plane,

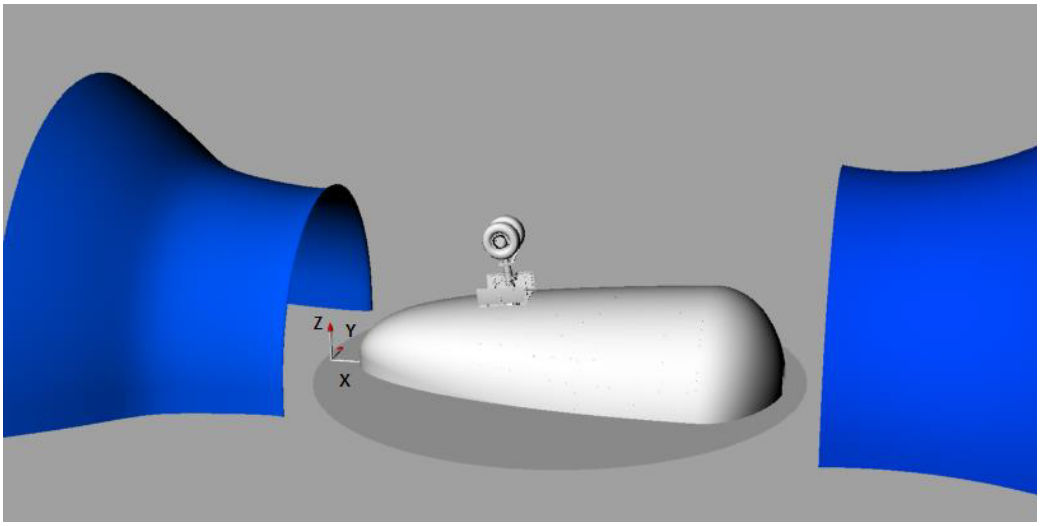

Fig. 1: Model and coordinate system inside the Pininfarina wind tunnel [49].

Fig. 2: ALLEGRA NLG model inside the wind tunnel with the top array visible [49].

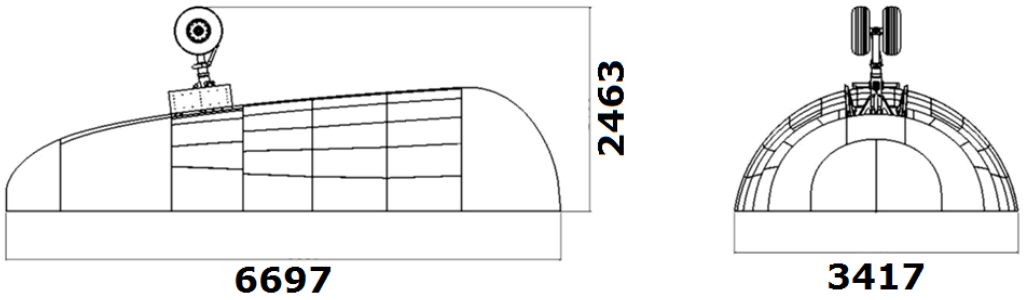

Fig. 3: Main dimensions of wind–tunnel test model in mm [49].

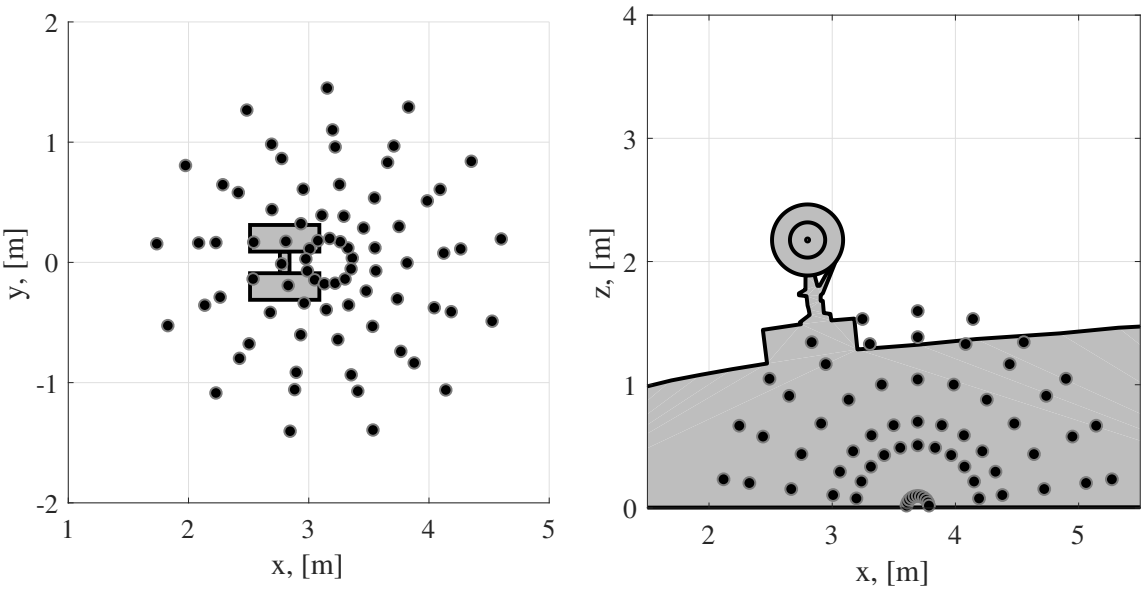

(a) (b)

Fig. 4: Microphone distribution for (a) the top array (b) the side array. A sketch of the ALLEGRA NLG model is plotted in gray for clarity reasons.

i.e. parallel to the model plane of symmetry and consisted of 66 microphones arranged in a half–wheel distribution with a diameter of approximately 3 m.

More details about the experimental setup can be found in [49].

The data of both arrays were acquired simultaneously at a sampling frequency of 32,768 Hz for 10 s per measurement. The time–averaged cross–spectral matrix (CSM) [50] was obtained by using frequency spectra processed with a block length of 8192 samples, Hanning windowing and 50% data overlap, providing a frequency resolution Δf of 4 Hz.

The frequency range of interest considered for postprocessing extends from 200 Hz to 4000 Hz. The lower limit was defined by the background noise and the spatial resolution of the array in order to properly separate the sound coming from the NLG model from other noise sources. The higher frequency limit was imposed by the minimum distance between microphones to prevent aliasing, the amount of sidelobes, and the signal–to–noise ratio.

B. Flyover measurements

A total of 115 aircraft flyovers in their landing stage were recorded at Amsterdam Airport Schiphol. Landing operations were preferred for this study because turbofan engines normally operate at lower power settings compared with takeoffs, making the identification of airframe noise sources (such as the NLG) more likely [30].

A phased microphone array consisting of 32 microphones distributed in a single–arm logarithmic spiral with a 1.7 m diameter was placed 1240 m away from the threshold of the Aalsmerbaan runway (36R), see Fig. 5c. An optical camera was fixed to the center of the array facing straight up, which provided video footage synchronized with the microphone data. The weather conditions during the measurements were very similar and presented low wind speeds [51].

Out of these 115 flyovers, 36 correspond to regional airliners (approximately 30% of the total), confirming the importance of regional flights at European airports. Data from three different regional aircraft types were selected, which are referred to henceforth as Aircraft Types A, B and C, respectively, for confidentiality reasons. The NLG systems from these aircraft types have a similar geometry as the ALLEGRA model tested in the wind tunnel and computational simulations aforementioned, as will be discussed in Sec. II D.

The array employed bandpass filters to obtain frequencies between 45 Hz and 11,200 Hz. A sampling frequency of 40 kHz was used. For each measurement, 0.1024 s of data was considered, for which the NLG is approximately overhead of the microphone array center (emission angle of $\theta \approx 90°$, corrected for the source motion). The averaged CSM [50] is computed employing data blocks of 2048 samples and Hanning windowing with 50% data overlap, providing a frequency resolution of approximately 20 Hz.

The frequency range selected for further analysis ranges from 1 kHz to 10 kHz. The lower bound

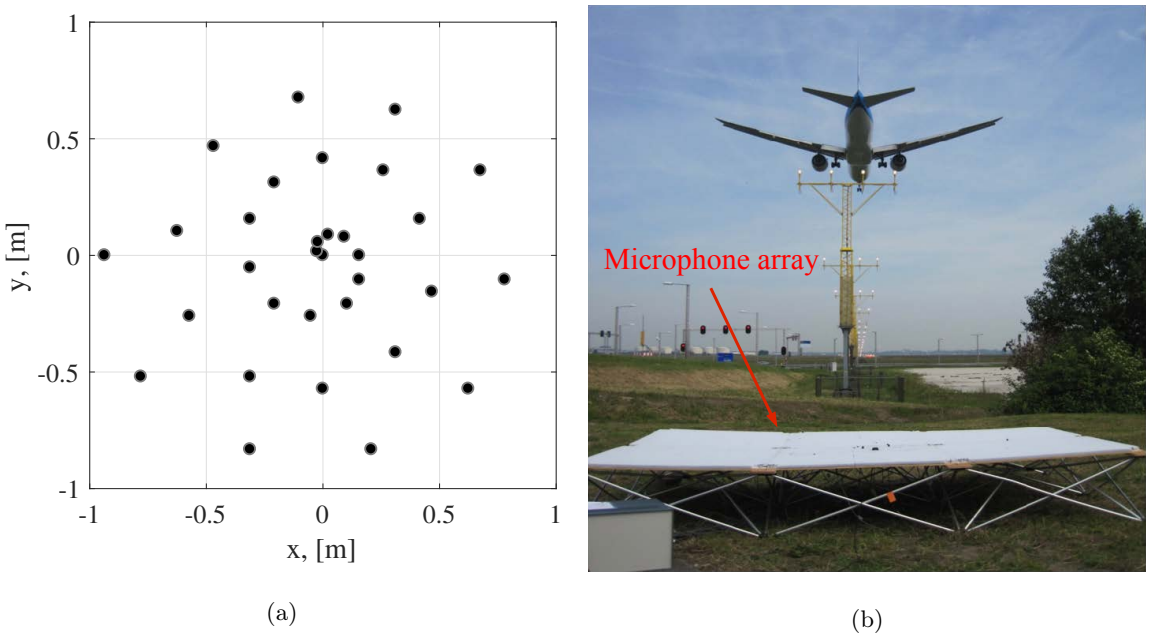

(a) (b)

(c)

Fig. 5: (a) Microphone distribution for flyover array. (b) Experimental setup [30]. (c) Location of the microphone array (red pin). The North points to the right [24].

was chosen for having enough spatial resolution to separate the sound coming from the NLG from other noise sources on board, such as the turbofan engines. For the three aircraft types selected, the minimum distance between NLG and engines ranged from 12 m to 20 m, approximately. Aircraft Types A and C are equipped with rear–mounted engines, which allows for an easier separation of the NLG noise contribution. Aliasing and the amount of sidelobes determined the highest frequency of study, as for the wind–tunnel case.

The aircraft trajectories were calculated to account for the propagation effects from the source to the receiver. Data from three different sources [30] were used:

1. The Automatic Dependent Surveillance–Broadcast (ADS–B) (when available).

2. The radar from air traffic control (provided by Amsterdam Airport Schiphol).

3. The extrapolation of the images taken by the optical camera.

The three methods provided very similar results (with variations up to 6%), but the data from the optical camera were employed due to its availability and because it is easier to overlay the acoustic source plots on the pictures. The results from the other two methods were used as a validation. The average flight altitude and aircraft velocity above the array for the aircraft studied in this paper were 65.7 m and 69.3 m/s, respectively. Henceforth, true air speeds (considering the wind velocities) are presented in this paper.

The Doppler effect was corrected according to Howell *et al.* [52] and the movement of the source was also later accounted for in the formulation of the beamforming algorithm [30, 53]. Finally, the geometrical spreading and the atmospheric absorption were also taken into account to obtain the L_{p} at the source position [2, 32]. A method for calculating the atmospheric absorption coefficient α per frequency was employed using the recorded ambient temperature and relative humidity [54].

C. Computational simulations

Compressible flow simulations were performed by Bouchouireb [33] using the commercial flow-solver STAR–CCM+ with an Improved Delayed Detached Eddy Simulation (IDDES) model [55]. A computational domain spanning 30 times the wheel diameter (d_{wheel}) in the streamwise direction, 18 d_{wheel} in the horizontal direction and 10 d_{wheel} in the vertical direction was used. Different mesh refinements were employed, with a higher grid density for meshes closer to the NLG smaller components [33]. The domain is discretized using an unstructured mesh with a total of 97 million hexahedral cells. The resolution of the mesh was sufficient to propagate the acoustic waves up to about 5000 Hz [33]. A detailed explanation about the computational setup and simulations is out of the scope of this paper. More information about the computational setup and the propagation analysis can be found in [33–35, 56].

The NLG geometry employed in the numerical simulations has been slightly simplified compared to the one used in the ALLEGRA wind–tunnel measurements: the bolts, nuts and air valves were

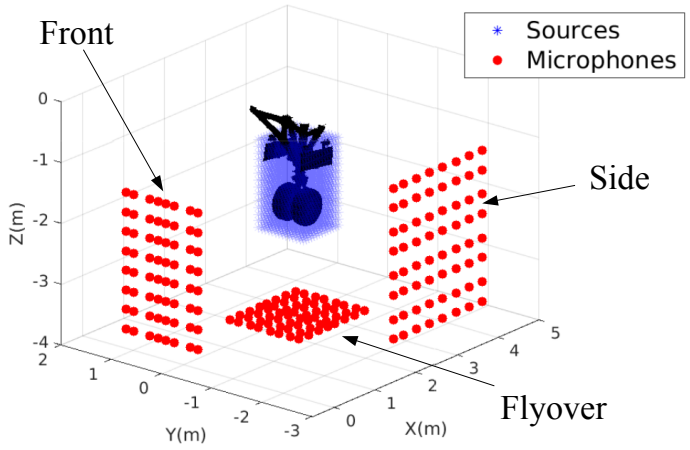

Fig. 6: Illustrative positions of the simulated ALLEGRA NLG model and the three virtual microphone arrays considered. The dimensions and distances are not representative of those used. Adapted from [33].

removed from the wheels, since they included details that were deemed too small to be correctly resolved by the computational grid and were replaced with coarser versions [33]. Moreover, small gaps between parts were filled, in particular the gap at the center of the rim was filled to approximate the wheel bearings. Lastly, the position of the whole model considered was flipped upside down in the z direction compared to the wind–tunnel tests, see Fig. 6. Henceforth, the z coordinates have been converted to positive values in the following discussions for an easier comparison. The fuselage belly was also included in the simulations, but is not illustrated in Fig. 6 for clarity reasons.

A uniform velocity field of $V = 50$ m/s was set at the inlet plane, a Dirichlet condition imposed the atmospheric pressure at the outlet plane and a no–slip condition was applied on the top plane of the computational domain, since it corresponds to the floor of the wind tunnel [33].

Five simulated acoustic arrays of 225 microphones each (distributed in square grids of 15×15) were considered in the computational domain, see Fig. 6. The microphone coordinates were approximated to the nearest cell center available in the mesh. These arrays were placed in the acoustic propagation region, outside the unsteady region close to the NLG surface, where hydrodynamical waves were dominant. Hence, it was considered that at the arrays' positions, the acoustic field was the dominating fluctuating field [33]. The relative positions of each array with respect to the NLG

model were:

1. *Flyover array*: Located at $z = 2.75$ m, i.e., 0.575 m away from the NLG axis, where the mesh spacing is 0.01 m.

2. *Side array 1*: Located at $y = -1$ m, i.e., 1 m away from the center of the NLG axis, where the mesh spacing is 0.02 m.

3. *Side array 2*: Located at $y = -0.4$ m, i.e., 0.4 m away from the center of the NLG axis, where the mesh spacing is 0.003 m.

4. *Front array 1*: Located at $x = 1.75$ m, i.e., 1.05 m away from the NLG axis, where the mesh spacing is 0.02 m.

5. *Front array 2*: Located at $x = 2.25$ m, i.e., 0.55 m away from the NLG axis, where the mesh spacing is 0.0025 m.

These positions do not correspond to those shown in Fig. 6 which are simply illustrative and not representative. Different scan planes (parallel to the corresponding array) were used, and will be specified when presenting the results in Sec. V. All the scan grids consisted of 961 scan points disposed in a square fashion (31×31).

Apart from the signals recorded at the microphones arrays, the propagated far–field signals using the Ffowcs Williams–Hawkings (FW–H) analogy [57] at observer positions located 1.5 m from the model in each of the three directions (flyover, side and front) were also considered.

The acoustic pressure data were extracted at all the microphone positions from 2500 samples at a sampling frequency of 20 kHz during 0.125 s (or 10 wheel convection cycles) [33]. The results were weighted using a Hanning windowing function and averaged using Welch's method [50], providing a frequency resolution of approximately 40 Hz.

D. NLG geometries

In this section, the NLG geometries of the ALLEGRA full–scale model tested in the Pininfarina wind tunnel and the computational simulations, and those of the three regional aircraft types selected are presented. All the considered NLG geometries consist of a bogie structure with a single axis and

Table 1: NLG geometry parameters [24].

Case	NLG type	d_{wheel} [m]	w_{wheel} [m]	d_{rim} [m]
Aircraft Type A	24 × 7.7 10 12 PR	0.610	0.196	0.286
Aircraft Type B	24 × 7.7 16 PR	0.610	0.196	0.406
Aircraft Type C	19.5 × 6.75 – 8	0.495	0.172	0.203
ALLEGRA	22 × 8.0 – 10	0.577	0.221	0.286

two wheels. Table 1 presents the dimensions of the wheel diameter d_{wheel}, wheel width w_{wheel} and rim diameter d_{rim} for the four NLG geometries (see Fig. 7), as well as the technical denomination of the NLG (following the ISO metric tire code for flotation sizes) in each case. All the dimensions listed in Table 1 present similar values. Such small differences in the size of the NLG are not expected to cause considerable changes in the L_{p} values radiated (less than 1 dB) [15, 37].

The NLG geometry designed within ALLEGRA, displayed schematically in Fig. 7, features a part of the fuselage, the gear bay, the doors and the gear assembly. The main elements of the NLG structure of the ALLEGRA model are depicted in Fig. 7 and listed with their names in Table 2.

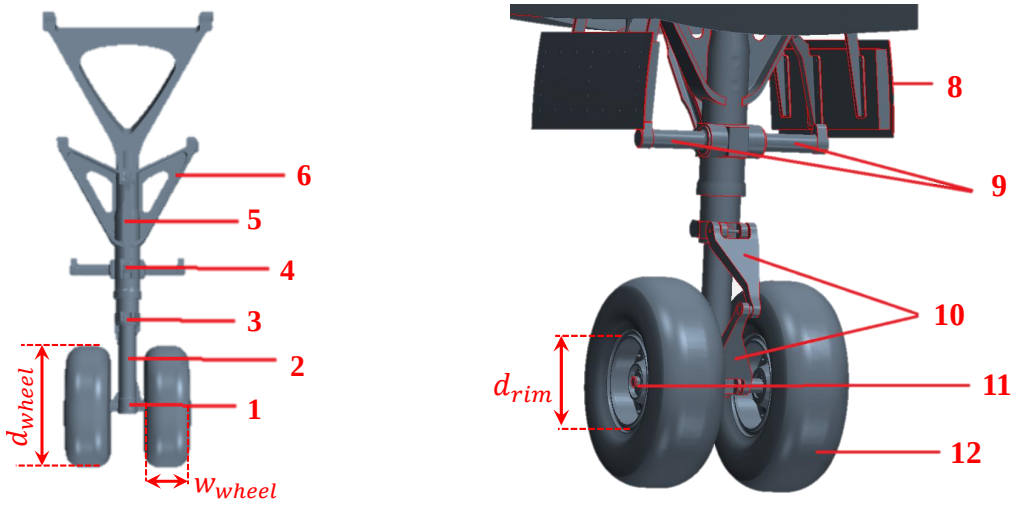

(a) (b)

Fig. 7: (a) Front and (b) back view of the NLG assembly. The list of elements corresponding to the numbers is in Table 2. Adapted from [33].

Table 2: Main elements of the landing gear. Extracted from [33].

Part Number	Part Name
1	Wheel axle
2	Main strut
3	Tow fitting
4	Lower arm joint
5	Drag stay lower arm
6	Main fitting
7	Drag stay upper panel
8	Bay door
9	Steering pinions
10	Torque link
11	Wheel hub
12	Wheel

III. Acoustic imaging methods

A. Method for the wind–tunnel experiments

Conventional frequency domain beamforming (CFDBF) [47] was applied to the acoustic data acquired by the top microphone array. The main diagonal of the CSM was removed in order to eliminate the influence of noise incoherent for all the microphones [53], such as the wind noise. The convection of the sound waves due to the flow velocity was considered. A standard shear layer correction, as outlined by Amiet [58], was applied. The beamforming results were integrated over a region of integration (ROI) covering the NLG position, following the approach of the Source Power Integration technique (SPI) [53, 59, 60]. The beamforming results were normalized by the integrated array response for a point source in the center of the ROI, also known as Point Spread Function (PSF). This way, more physical results are obtained, because the influence of the array's geometry in the L_p results is reduced [43, 53, 61–64] and the source plots are brought back to a single sound pressure level.

In addition, the high–resolution deconvolution method HR–CLEAN–SC [47, 65–68] was also

applied to the data from both arrays in order to obtain a better dynamic range (fewer and lower sidelobes) and to investigate whether one or more sound sources were present (even beyond the Rayleigh resolution limit [65–67]). For the frequency range considered in the wind–tunnel measurements (200 Hz to 4 kHz), the differences between the obtained spectra by the SPI technique and HR–CLEAN–SC were small. Henceforth, the spectra obtained with HR–CLEAN–SC are presented in this paper.

B. Method for the flyover measurements

Functional beamforming [69, 70] was selected in this case, as it provides better dynamic range and array spatial resolution than CFDBF, and these features are very important for flyover measurements, due to the relatively large distance between source and observer [30, 32, 45]. Comparative studies with other acoustic imaging methods showed that functional beamforming [30, 47] provides better results when applied to flyover measurements.

The de–Dopplerized acoustic signals were employed and the movement of the source was taken into account in the beamforming formulation [30, 53, 71]. Removing the main diagonal of the CSM for this algorithm is prone to significant errors, since the method relies on the eigenvalue decomposition of the CSM [72]. For this experiment, however, the diagonal removal approach was not considered to be necessary, due to the low wind speeds and low background noise levels [30]. This method basically raises the CFDBF source plot to the power of an exponent parameter ν and the CSM to the inverse of this power $\frac{1}{\nu}$. The value of ν in this study was chosen to be 32 after performing a sensitivity analysis [30, 45].

Additionally, the source maps were integrated over an area of interest located at the NLG position for each case (see Fig. 10). The process is similar to the SPI technique aforementioned in Sec. III A, where the beamforming results are now normalized by the PSF at the center of the integration area provided by functional beamforming.

C. Method for the computational simulations

The acoustic data extracted from the flow computations was propagated to the simulated microphone arrays and processed using several beamforming approaches [33]. In this paper only results

obtained with an adapted version of Linear Programming Deconvolution (LPD) [73], called dual–LPD [56], are presented. This method is essentially an alternative version of solving the inverse problem considered in deconvolution methods such as DAMAS [74], but using linear programming. Deconvolution methods typically offer better dynamic range and spatial resolution than CFDBF, but require longer computational times.

Unfortunately, the absolute spectra obtained by the simulated microphone–array measurements were not available due to confidentiality reasons. Hence, only source maps depicting the location of the identified sound sources and two far–field sound spectra are presented in this manuscript for comparison purposes.

IV. Noise prediction models

This section briefly describes three common airframe noise prediction models currently used to predict LG noise. The focus is kept on semi–empirical and semi–analytical noise models typically used for fast estimations of aircraft noise during aircraft design and parametric sensitivity studies to quantify variations in the noise impact due to changes in the aircraft geometry. These models are typically developed based on wind–tunnel or flight measurements of several aircraft and are averaged or normalized to reflect the typical noise spectra and directivities of generic aircraft geometries. As such, their accuracy is limited to the small range of the measurement database on which they are based on. Nonetheless, the models described here have been used extensively by organizations worldwide to assess the community noise impact of various aircraft designs, as well as flight procedures and routes. The computational efficiency of the models to compute the noise impact, in the range of seconds for selected observer points and minutes for ground grids needed to make noise contours, has led to their continuing, widespread use in the noise modeling and prediction communities. Three of the most frequently used models for predicting landing gear noise, those of Fink [22], Guo [37, 41], and DLR [21] are explained here. Whereas these three methods were developed using data of larger aircraft, they all include scaling factors considering the geometry features of the NLG, thus, they should be suitable for smaller NLG systems, such as those from regional aircraft considered in this study. It should be noted that the models of Fink and Guo use imperial units, e.g., inches for lengths and knots for the velocity.

A. Fink's model

Fink's method [22] was developed for the US Federal Aviation Agency (FAA) and has been implemented in NASA's Aircraft Noise Prediction Program (ANOPP) framework [75, 76]. Fink assumes that there are two primary noise sources on the landing gear: the strut and the wheels, based on experimental data from flyover measurements of several aircraft, mostly from the Boeing company [4]. Therefore, the input parameters required for this method are simply the mean flow velocity V, the number of wheels N_{wheel}, the wheel diameter d_{wheel} and the strut length l_{strut}. The various interaction effects of the wheels and strut with each other, as well as with other airframe components, are only accounted for by the use of empirical fitting factors. The generic form of the mean–squared, far–field acoustic pressure (in one–third–octave bands) for all airframe noise components according to Fink's method is given by

$$\left\langle p^2 \right\rangle = \frac{\rho c P \hat{D} \hat{F}}{4\pi r^2 \Big[1 - M\cos\left(\theta\right)\Big]^4}, \tag{1}$$

where ρ is the air density, c is the speed of sound, P is the sound power of each component (wheel and strut), $\hat{D}$ is the directivity function, $\hat{F}$ is the spectrum function and r is the distance between source and observer. The term between brackets $\Big[1 - M\cos\left(\theta\right)\Big]^4$ is the convective amplification factor due to the motion of the source [30], where M is the Mach number: $M = V/c$, where V is the source velocity.

The sound power for the wheel noise is defined as

$$P_{\text{wheel}} = K_1 M^6 N_{\text{wheel}} d_{\text{wheel}}^2, \tag{2}$$

where $K_1 = 4.349{\times}10^{-4}$ lb^2/s^4 for two–wheel LG systems (typically for NLG) and $K_1 = 3.414{\times}10^{-4}$ lb^2/s^4 for four–wheel LG systems (typically for MLG). The term M^6 refers to the expected 6^{th} power law with the flow velocity [77].

The sound power for the strut noise is defined as

$$P_{\text{strut}} = K_2 M^6 d_{\text{wheel}} l_{\text{strut}}, \tag{3}$$

where $K_2 = 2.753 \times 10^{-4}$ lb^2/s^4. The contributions of both components are typically of comparable order of magnitude.

The directivity functions for each component are calculated using

$$\hat{D}_{\text{wheel}} = \frac{3}{2} \sin^2 \theta, \tag{4}$$

$$\hat{D}_{\text{strut}} = 3 \sin^2 \theta \sin^2 \phi, \tag{5}$$

where θ is the polar emission angle and ϕ is the azimuthal sideline noise emission angle [22]. The case of $\phi = 0°$ corresponds to the direction directly under the landing gear and $\phi = 90°$ corresponds to the wheel axis pointing to the right. With this angle criteria, and according to Eq. (5), the strut does not contribute to the overall noise emissions directly under the landing gear ($\phi = 0°$).

The spectrum function $\hat{F}$ depends on the component and N_{wheel}, as well as on the Strouhal number based on the wheel diameter [22], $St = \frac{f d_{\text{wheel}}}{c}$. Equation (6) below represents the spectrum function depending on several empirical parameters ($\hat{A}$, $\hat{B}$, $\hat{q}$, $\hat{\mu}$ and $\hat{\sigma}$), which can be found for each component in Table 3 for the cases with two and four wheels per bogie.

$$\hat{F} = \frac{\hat{A} St^{\hat{\sigma}}}{(\hat{B} + St^{\hat{\mu}})^{\hat{q}}}, \tag{6}$$

Table 3: Required empirical parameters for Fink's noise prediction method [76].

Component	$\hat{A}$	$\hat{B}$	$\hat{q}$	$\hat{\mu}$	$\hat{\sigma}$
Wheel ($N_{\text{wheel}} = 2$)	13.58	12.5	2.25	2	2
Wheel ($N_{\text{wheel}} = 4$)	0.0577	1	1.5	2	2
Strut ($N_{\text{wheel}} = 2$)	5.325	30	1	8	2
Strut ($N_{\text{wheel}} = 4$)	1.28	1.06	3	2	3

Hence, the total LG noise emissions can be calculated by summing the respective contributions of the wheel assembly and the strut by introducing Eqs. (2) to (6) into Eq. (1).

B. Guo's model

Also known as the "Boeing" method, Guo's method [37, 41] is based on fundamental aerodynamic noise theory and scaling laws adjusted to fit full–scale LG aeroacoustic tests mostly from Boeing aircraft [38]. In order to include more physics than Fink's method, this technique considers three different types of LG components depending on their size, each of them contributing in a different frequency range:

1. **Large–scale structures** such as the wheels, contributing to the low–frequency noise.

2. **Mid–scale structures** such as the main struts, contributing to the mid–frequency noise.

3. **Small–scale structures** such as the hydraulic lines and LG dressings, contributing to the high–frequency noise.

These three types of components are considered separately, each with a different spectral shape and directivity. For this purpose, more detailed geometrical inputs of the LG are required for this method, compared to Fink's method. Hence, Guo's method is expected to provide higher–fidelity noise predictions.

The far–field mean–squared acoustic pressure can be estimated as

$$\langle p^2 \rangle = \frac{\rho^2 c^4 M^6 \hat{D}_{\text{overall}}}{r^2 \Big[1 - M\cos(\theta)\Big]^4} \big(P_{\text{low}} + P_{\text{mid}} + P_{\text{high}}\big), \tag{7}$$

where P_{low}, P_{mid} and P_{high} represent the sound powers terms of the low, mid and high frequency components, respectively. It should be noted that the dimensions of these P terms are of surface area (see Eq. (9) below), but they become of acoustic power (Pa^2) after multiplying them by the $\rho^2 c^4 / r^2$ term. The term $\hat{D}_{\text{overall}}$ is the overall directivity function, in addition to the directivity function included in each P term, which accounts for the installation effects of the LG. The presence of the wing and fuselage of the aircraft causes reflection and diffraction [37], which will enhance the noise radiation, especially in the overhead direction ($\theta = 90°$). This parameter can be estimated using the following empirical expression

$$\hat{D}_{\text{overall}} = 1.2(1 - 0.9\cos^2\theta)^2. \tag{8}$$

Each of the P terms in Eq. (7) are defined as

$$P = \hat{\beta} S \hat{D} \hat{F}, \tag{9}$$

where $\hat{\beta}$ is the flow energy conversion efficiency parameter (see Table 4) and S is the aggregate surface integration effects term [37], which depends on the geometry of the LG components:

$$S_{\text{low}} = \pi N_{\text{wheel}} w_{\text{wheel}} d_{\text{wheel}}, \tag{10}$$

$$S_{\text{mid}} = \sum_{k=1}^{N_{\text{strut}}} \hat{s}_{\text{strut},k} l_{\text{strut},k}, \tag{11}$$

$$S_{\text{high}} = \hat{\eta} l_{\text{high}}^2, \tag{12}$$

where w_{wheel} is the wheel width, N_{strut} is the number of main struts in the LG assembly, $\hat{s}_{\text{strut},k}$ and $l_{\text{strut},k}$ are the perimeter of the cross section and the length of the k^{th} strut, respectively. The dimensionless parameter $\hat{\eta}$ is the complexity factor accounting for the geometric complexity of the small–scale components of the LG. This parameter has a complicated expression depending on the takeoff weight of the aircraft, but for NLG, $\hat{\eta}$ can be approximated by a constant value of 0.1 [37], since a typical NLG is much simpler than a MLG and their complexity does not vary significantly within different aircraft types. The characteristic length of the small–scale components l_{high} can be approximated as

$$l_{\text{high}} = 0.15 \frac{S_{\text{mid}}}{\pi \sum_{k=1}^{N_{\text{strut}}} l_{\text{strut},k}}. \tag{13}$$

A different Strouhal number is defined for each frequency range:

Table 4: Required empirical parameters for Guo's noise prediction method [37].

Frequency	$\hat{A}$	$\hat{b}$	$\hat{B}$	$\hat{h}$	$\hat{q}$	$\hat{\beta}$	$\hat{\mu}$	$\hat{\sigma}$
Low	3.53	3	0.62	0.2	2.6	4.5×10^{-8}	2.5	4
Mid	0.42	2	0.18	0.6	4.2	1.5×10^{-8}	1.5	3
High	0.08	0.1	0.1	1	4.2	3.2×10^{-5}	1.1	2

$$St_{\text{low}} = \frac{f d_{\text{wheel}}}{V}, \tag{14}$$

$$St_{\text{mid}} = \frac{f S_{\text{mid}}}{\pi V \sum_{k=1}^{N_{\text{strut}}} l_{\text{strut},k}}, \tag{15}$$

$$St_{\text{high}} = \frac{f l_{\text{high}}}{V}. \tag{16}$$

The spectrum function $\hat{F}$ can be calculated in the same way as for Fink's method (see Eq. (6)) using the parameters gathered in Table 4.

The frequency–dependent directivity function $\hat{D}$ can be defined as

$$\hat{D} = (1 + \hat{h}\cos^2\theta)^2 (1 + \hat{b}\sin^2\phi)^2, \tag{17}$$

where $\hat{h}$ and $\hat{b}$ are empirical constants [38] whose values are listed in Table 4. This directivity pattern peaks at the upstream and downstream directions and shows a minimum near the overhead direction ($\theta \approx 90°$). Moreover, as the frequency increases, the radiation pattern becomes more directional in the polar direction [37]. In the azimuthal direction, the maximum emission direction corresponds to $\phi = 90°$.

The effect of the lower flow velocity impinging at the MLG compared to the NLG is also accounted for [20]. With all these equations, all the P terms in Eq. (7) can be calculated and the far–field noise emissions can be obtained.

The predictions of this method have been shown to compare well with experimental data from wind–tunnel and flight measurements [37, 38], both in parametric trends and absolute noise levels.

C. DLR's model

Unlike, Fink's and Guo's models which were mainly developed using data from Boeing aircraft, the airframe noise prediction model of DLR is based on data from the Airbus A320 family [21]. This method forms part of the aircraft system noise prediction tool called the Parametric Aircraft Noise Analysis Module (PANAM) [78, 79], which models the overall aircraft noise as a sum of individual noise components on–board and their interactions. This information is then used to assess the ground noise impact of the whole aircraft. In essence, PANAM is relatively similar to ANOPP in the noise generation mechanisms it considers and the way it estimates the aircraft noise levels [80].

The implemented noise source models for landing gear noise simulate the noise emission according to specific geometry parameters, installation effects and flow conditions. PANAM considers the noise emissions of both the MLG and the NLG, but for this study, only the calculations regarding the NLG are employed. The landing gear is modelled as a non–directional source, i.e., the directivity function $\hat{D}$ previously defined in the models of Fink and Guo would have a value of 1 for all directions.

The geometry of the NLG is taken into account in the following term:

$$\Delta L_{\mathrm{p,geo}} = 10 \log_{10} \left(\frac{l_{\mathrm{strut}} \, \delta \, d_{\mathrm{wheel}} \sqrt[4]{N_{\mathrm{axles}}}}{r^2} \right), \tag{18}$$

where δ is the gear extraction factor between 0 (retracted) and 1 (extended, as in this study) and N_{axles} is the number of axles, which is an indicator of the overall complexity of the landing gear.

The local flow conditions at the NLG are accounted for with the following expression that follows the 6^{th} power law with the flow velocity [77] with respect to a reference velocity of $V_{\mathrm{ref}} = 100$ m/s:

$$\Delta L_{\mathrm{p,vel}} = 60\ \log_{10}\left(\frac{V}{V_{\mathrm{ref}}}\right), \tag{19}$$

Lastly, a spectral shape function is applied depending on the Strouhal number based on a reference distance of 1 m $St = f \cdot 1/V$:

$$\Delta L_{\mathrm{p,spec}}(St) = \begin{cases} \log_{10} St^{1.1143} & \text{for } St \leq 10 \\ 10.45 + \log_{10} St^{-9.3367} & \text{for } St > 10 \end{cases} \tag{20}$$

The total sound pressure level (L_{p}) spectra of the NLG is calculated as a sum of all these contributions plus an additional normalized level based on an empirical constant of 110 dB.:

$$L_{\mathrm{p}} = 110 + \Delta L_{\mathrm{p,geo}} + \Delta L_{\mathrm{p,vel}} + \Delta L_{\mathrm{p,spec}}(St), \tag{21}$$

The predictions of this method have been previously compared with flyover measurements under operational conditions featuring Airbus A320 aircraft [23, 80].

V. Results

A. Acoustic imaging results

The acoustic imaging results obtained can be divided in three categories depending on the emission direction considered, see Fig. 6:

1. Flyover (in the z direction, as considered for the flyover measurements).

2. Side (in the y direction).

3. Front (in the x direction).

All the source maps presented in this paper present relative L_{p} values with respect to the peak value in each map ($L_{\mathrm{p,max}}$).

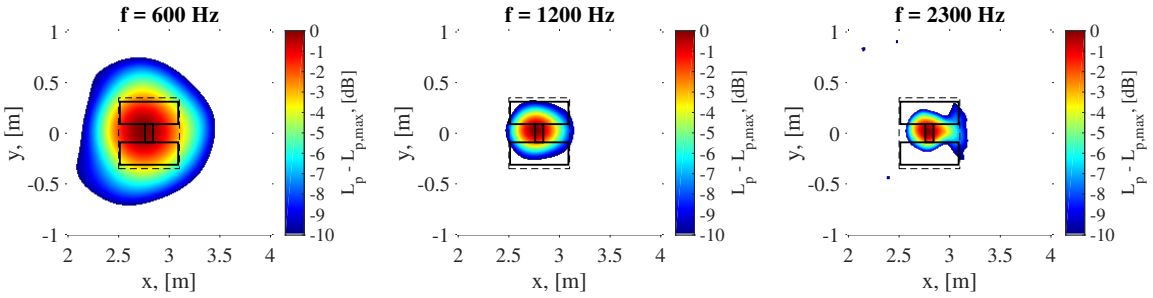

(a) (b) (c)

Fig. 8: CFDBF source plots for the ALLEGRA NLG wind–tunnel model (*flyover* view) for $V = 50$ m/s. The NLG model is depicted as solid black lines.

1. *Flyover direction*

Figure 8 depicts three CFDBF source plots of the ALLEGRA NLG corresponding to the wind–tunnel measurements with a flow speed of 50 m/s and one–twelfth–octave bands with center frequencies of 600 Hz, 1200 Hz and 2300 Hz, respectively. The scan plane used was parallel to the top microphone array, at a distance of 1.825 m from it (i.e., at $z = 2.175$ m, containing the wheel axis). Figure 9 contains the results corresponding to the same conditions as in Fig. 8 after applying HR–CLEAN–SC, which offers clearer source plots. The dashed rectangle denotes the ROI. In both figures, it seems that the dominant noise source for all frequency cases is located between both wheels. The position is slightly shifted upwind from the center of the wheel axis, which could be caused by an error when determining V in of the wind tunnel. However, sound sources could be located anywhere along the vertical line passing through the middle point of the axis, since the resolution of the microphone array in the normal direction (z direction) is not accurate enough to localize the source within the axis. Thus, it is also possible that the main sound source is located on the strut of the NLG or thereabouts.

Figure 10 illustrates a functional beamforming source plot for an example flyover measurement of each of the three aircraft types aforementioned. It is observed that the NLG is always the dominant noise source for the frequency range selected (one–third octave band centered at 2 kHz). This frequency band was selected due to the presence of strong tonal noise, as it will be shown

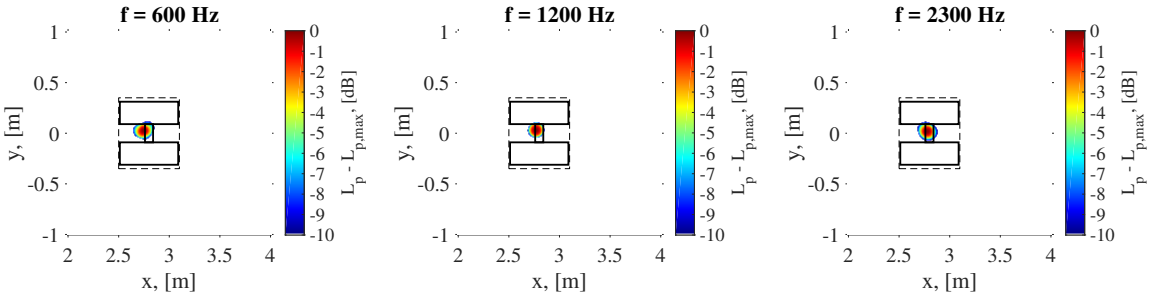

(a) (b) (c)

Fig. 9: HR–CLEAN–SC source plots for the ALLEGRA NLG wind–tunnel model (*flyover* view) for $V = 50$ m/s. The NLG model is depicted as solid black lines.

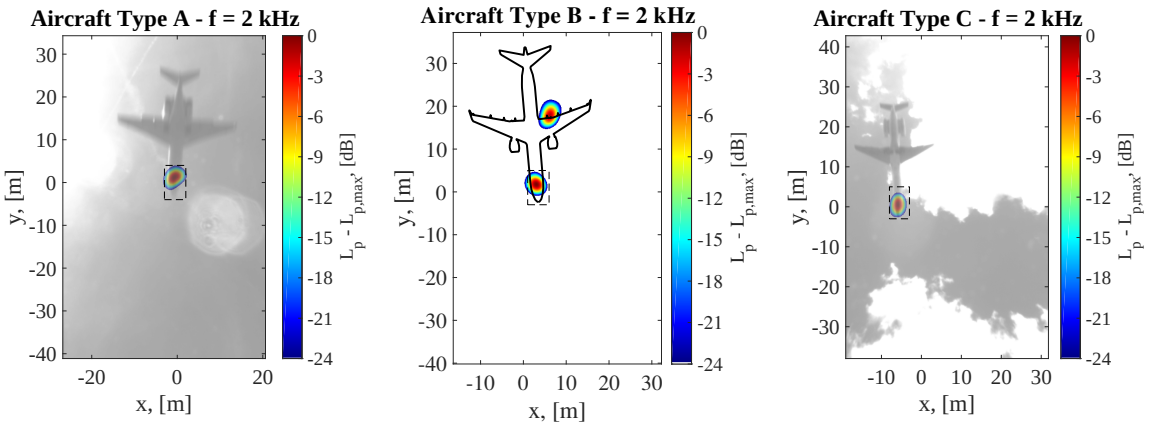

(a) (b) (c)

Fig. 10: Functional beamforming (with $\nu = 32$) source plots for each aircraft type for 2 kHz.

in Sec. V B. The dashed rectangles again denote the ROIs. For Aircraft Type B (Fig. 10b) an additional sound source is localized at what appears to be the flap side edge of the left wing. For this example, the outline of the aircraft has been manually added for clarity, because the sunshine blurred the picture.

Two source plots obtained from the computational simulations in the flyover direction with the *Flyover* array are depicted in Fig. 11 for the one–twelfth–octave band with center frequencies of 1200 Hz and 2300 Hz, respectively. The scan plane was located at $z = 2.5$ m. Although the source plots obtained by dual–LPD present a more *discontinuous* distribution, the locations of the dominant sound sources agree with those found in the wind–tunnel experiments, see Figs. 8 and 9,

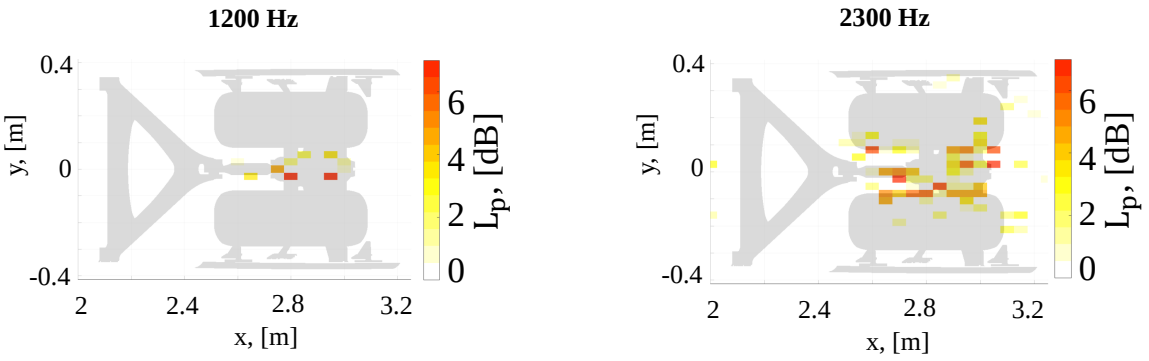

(a) (b)

Fig. 11: Dual–LPD source plots for the computational simulations (*flyover* view) with $V = 50$ m/s at (a) 1200 Hz and (b) 2300 Hz. Adapted from [33].

i.e., between both wheels.

2. Side direction

The source plots corresponding to the side array in the ALLEGRA wind–tunnel experiments are presented in Figs. 12 and 13, for CFDBF and HR–CLEAN–SC, respectively. The same conditions as in Figs. 8 and 9 are considered (a flow speed of 50 m/s and one–twelfth–octave bands with center frequencies of 600 Hz, 1200 Hz and 2400 Hz). The scan plane used was parallel to the side microphone array, at a distance of 4.2 m from it (i.e., at $y = 0$ containing the center of the wheel axis).

Once again, HR–CLEAN–SC provides clearer source plots, which are used to determine the location of the dominant sound sources. For the 600 Hz frequency band, it seems that one of the dominant sound sources is located close to the rim of the wheel, next to the wheel axle. For the frequency bands centered at 1200 Hz and 2400 Hz, the main noise source seems to be located near the tow fitting and torque link, respectively (see Fig. 7). The presence of the wheels might shield potential sources located exactly at the axle in the *side* direction. For this emission direction, two different ROIs were defined (indicated as dashed rectangles in Figs. 12 and 13), one covering the wheel and the other covering the main strut and the bay door. This way, the contributions of each region can be separated.

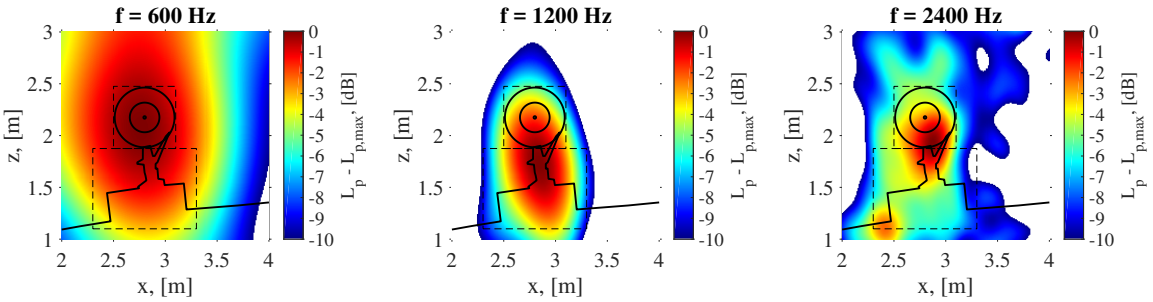

Fig. 12: CFDBF source plots for the ALLEGRA NLG wind–tunnel model (*side* view) for $V = 50$ m/s. The NLG model is depicted as solid black lines.

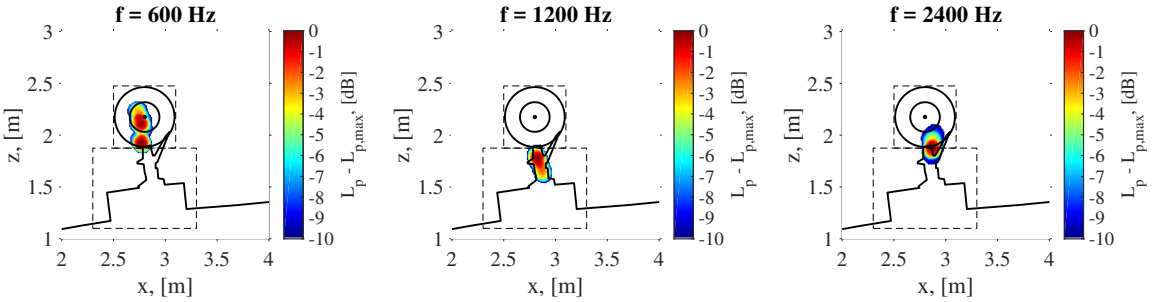

Fig. 13: HR–CLEAN–SC source plots for the ALLEGRA NLG wind–tunnel model (*side* view) for $V = 50$ m/s. The NLG model is depicted as solid black lines.

Figure 14 contains two source plots obtained from the computational simulations in the side direction for the one–twelfth–octave band with center frequencies of 1200 Hz and 2400 Hz, obtained by the *Side array 1* and the *Side array 2*, respectively. The scan plane was located at $y = -0.3$ m. For the band centered at 1200 Hz, the sound sources seem to be clustered along the tow fitting, the lower arm joint and the torque link, which agrees with the wind–tunnel results. For the case of 2400 Hz, on the other hand, the dominant sound source is located at the upwind part of the bay door. This source at the bay door was also present in the CFDBF results for the wind–tunnel experiment (see Fig. 12c), but was deemed to be a sidelobe by HR–CLEAN–SC (see Fig. 13c).

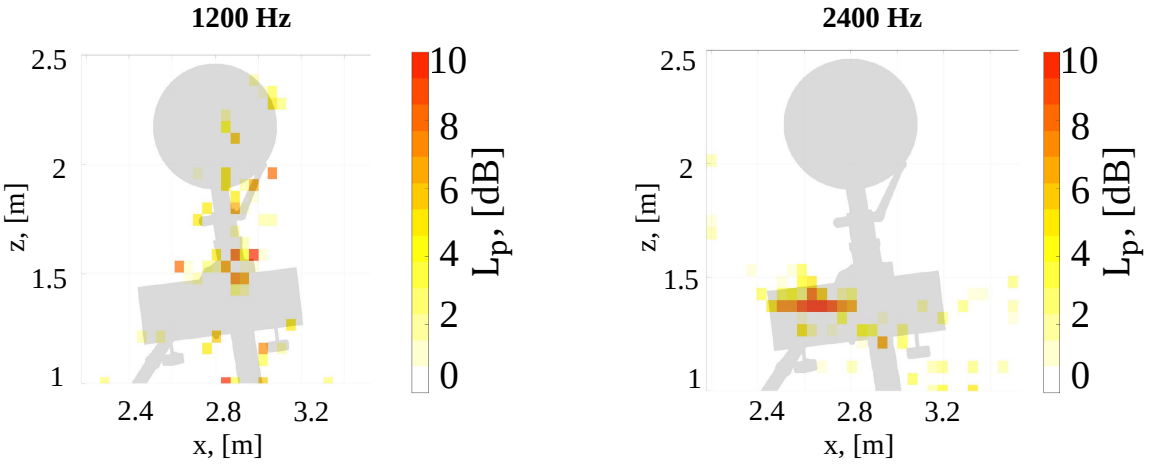

(a) (b)

Fig. 14: Dual–LPD source plots for the computational simulations (*side* view) with $V = 50$ m/s at (a) 1200 Hz and (b) 2400 Hz. Adapted from [33].

3. *Front direction*

As aforementioned, the computational simulations allow for the non–intrusive placement of virtual microphone arrays to study emission directions that would be impractical to measure in wind tunnels. Figure 15 shows the simulated source plots in the front direction for one–twelfth–octave band with center frequencies of 1000 Hz and 2400 Hz obtained by the *Front array 1* and *Front array 2*, respectively. The scan plane was located at $x = 2.826$ m. For the first case, the strongest noise source is located in the center of the wheel axle, whereas for the second band, the sources are more spread in the center of the wheel axle, the lower arm joint and the bay doors. The bay door was also a dominant noise source for the side direction at that frequency, see Fig. 14b.

B. Frequency Spectra Comparison

1. *Correlation with flow velocity*

As discussed in the literature, it is generally agreed that the aerodynamic noise generated by a landing gear is a result of dipole–type pressure fluctuations due to unsteady pressure forces with a maximum emission direction perpendicular to the flow direction and to the main strut. The theory of Curle [77] shows that, in such instances, the acoustic intensity is proportional to V^6. For the

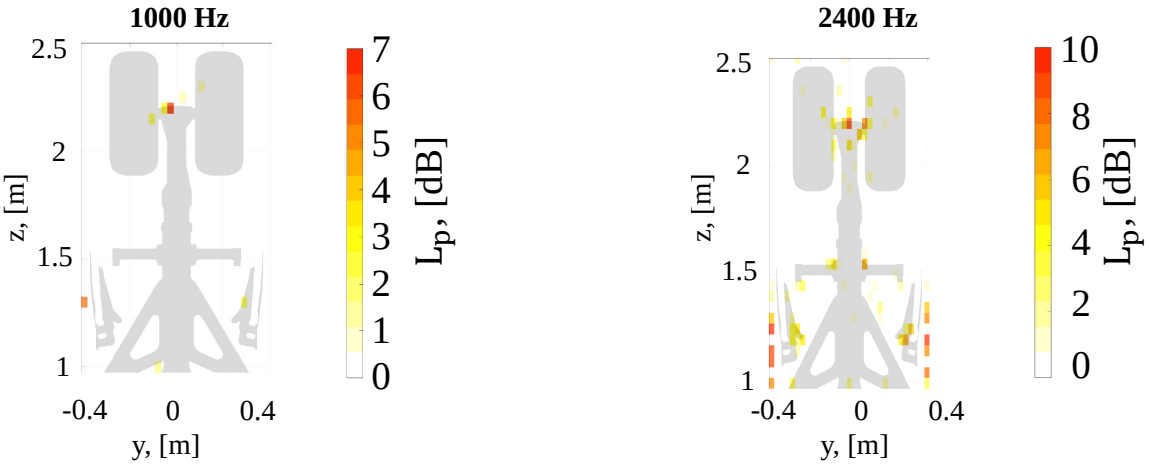

(a) (b)

Fig. 15: Dual–LPD source plots for the computational simulations (*front* view) with $V = 50$ m/s at (a) 1000 Hz and (b) 2400 Hz. Adapted from [33].

sound pressure level L_{p} (in logarithmic scale) the scaling can be performed using

$$L_{\mathrm{p,V}} - L_{\mathrm{p,V_{ref}}} \approx 60 \log\left(\frac{V}{V_{\mathrm{ref}}}\right) \tag{22}$$

where V_{ref} denotes an arbitrary reference velocity.

Regarding the ALLEGRA model, a previous experimental study [24] showed that it and the Aircraft Type A follow power laws with respect to the flow velocity with exponents of 5.90 and 5.93, respectively, concurring well with other studies to be found in the literature [5, 12, 15, 22].

In this study, given that a range of velocities was examined, an amplitude scaling was also conducted. An illustrative example is presented in Fig. 16, where the integrated HR–CLEAN–SC narrow–band frequency spectra for the ALLEGRA model in the flyover direction for the four flow velocities are presented. The background noise levels of the wind tunnel (with only the fuselage belly present in the test section, but without the NLG) for each flow velocity are presented in the same figure for reference. A signal to noise ratio between 5 dB and 30 dB is observed within the frequency range of interest. When the spectra are scaled following the 6^{th} power law and taking 40 m/s as the reference velocity V_{ref}, all the spectra collapse well at mid-frequencies in one single line, see Fig. 17a. All the spectra are mostly broadband above 600 Hz. The low frequency tonal content

of these spectra does not scale, and is the subject of different studies [19, 28] which examine the tonal contribution of the wheel bay and LG components in that frequency range.

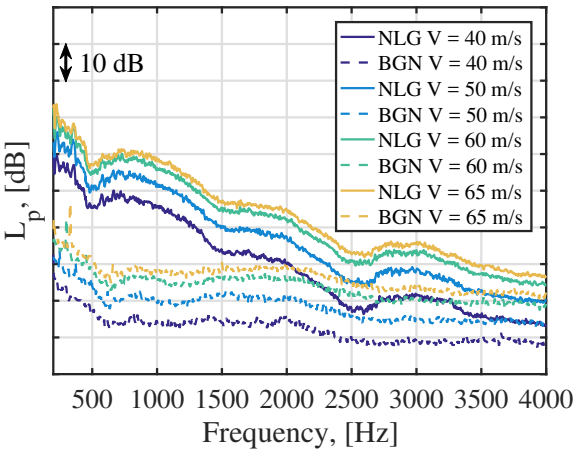

Fig. 16: Narrow–band spectra for each velocity of the ALLEGRA NLG wind–tunnel model in the flyover direction. The background noise (BGN) is plotted with dashed lines.

Referring again to Fig. 17a, the collapse seems to be less satisfactory for frequencies higher than 1.2 kHz. Curle's theory only holds true when the sound sources are compact, i.e., the relationship is true only when the geometric size of the sound source is small when compared to the acoustic wavelength. Guo *et al.* [81] and Bennett *et al.* [28] demonstrated that this assumption is no longer valid for the small details in the landing gear, such as dressings, small details, rods, fixtures, etc. These small details generate higher–frequency noise and, thus, the wavelength is no longer large compared to the noise sources and can no longer be considered to be compact. Instead of surface pressure fluctuations, they discuss that the noise sources are instead radiated from the turbulent flow which surrounds the small features of the landing gear and, hence, the velocity requires a scaling exponent of a higher order. Figure 17b, shows the curves scaled to the velocity to the seventh power, and above 1.2 kHz there seems to be a more satisfactory collapse. Given the high level of detail of the manufactured NLG model, it is not just the additional dressings and fixtures, as, in Guo *et al.* [81], that is contributing to this high-frequency noise, but all the small features to be found such as the hinges, wheel hub detail, fixtures, rods, ribs, pins, gussets, etc.

Very similar results were obtained for the side emission direction, see Figs. 18a and 18b for a scaling of the spectra using V^6 and V^7, respectively. Once again, no important tonal peaks were

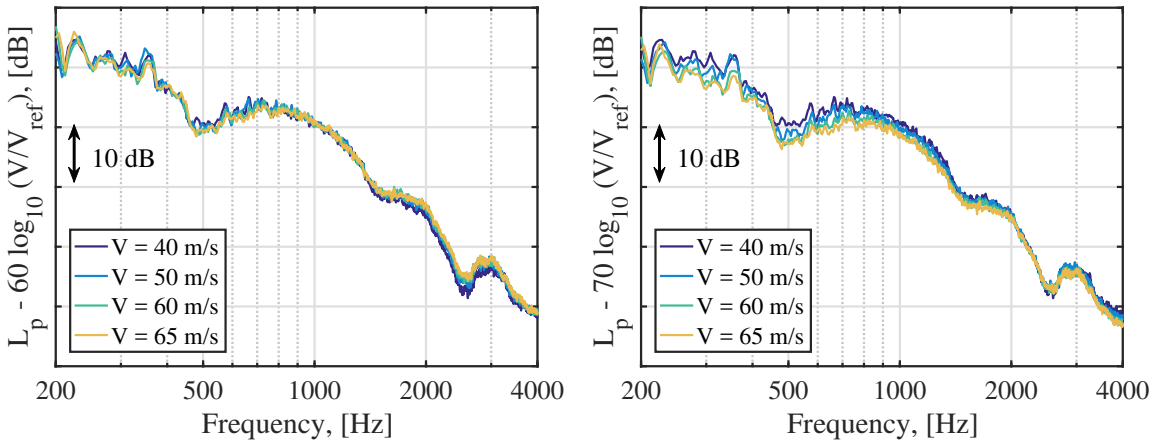

(a) (b)

Fig. 17: Scaled frequency spectra for each velocity of the ALLEGRA NLG wind–tunnel model in the *flyover* direction, using (a) V^6 and (b) V^7. ($V_{\text{ref}} = 40$ m/s).

observed.

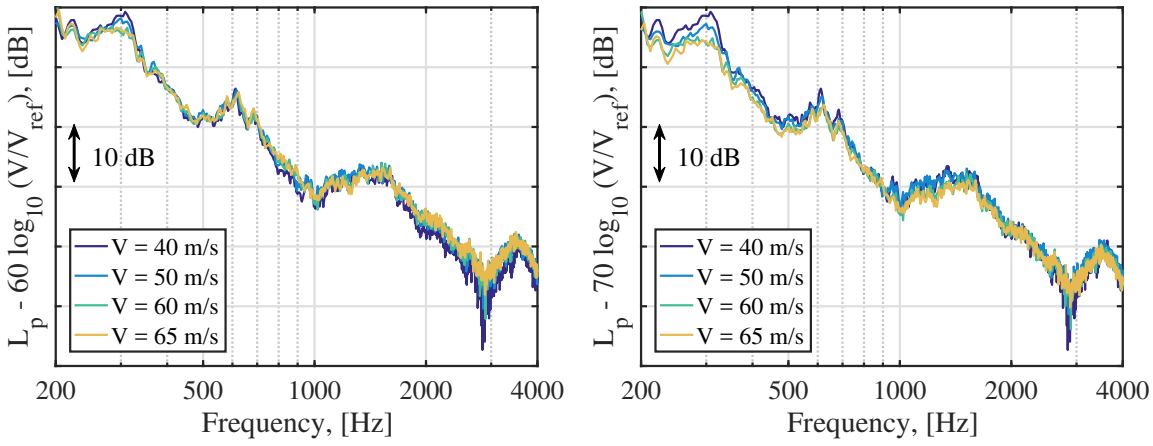

(a) (b)

Fig. 18: Scaled frequency spectra for each velocity of the ALLEGRA NLG wind–tunnel model in the *side* direction, using (a) V^6 and (b) V^7. ($V_{\text{ref}} = 40$ m/s).

The change of the velocity exponent that provides the best fit for the spectra for the various frequency ranges is better illustrated in Fig. 19. These values were obtained by using a linear least–squares fit to the sound levels for each band and the four flow velocities available. In this figure, it is observed that after the band centered in 1250 Hz, the values of the velocity exponent increase

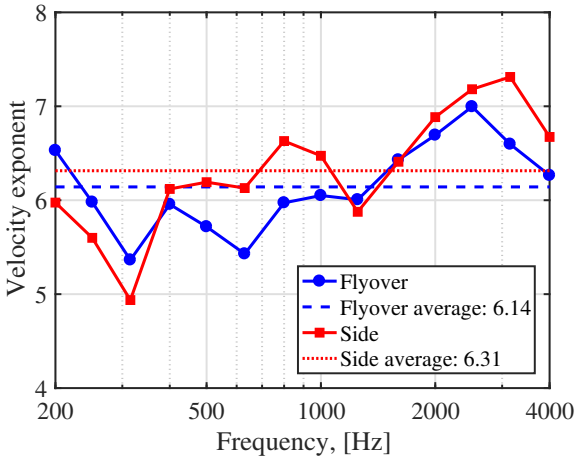

Fig. 19: Estimations of the exponent for the power law with the flow velocity for the flyover and side emission directions for the ALLEGRA NLG wind–tunnel model.

considerably up to values around 7. The average values of the velocity exponent (6.14 and 6.31 for the flyover and side direction, respectively) are, however, still close to the value of 6 suggested by Curle.

From this section we see that a scaling with V^6 is robust but in some higher frequency ranges a scaling with V^7 may also be considered to be more accurate. Similar results were found by Liu *et al.* [82] when measuring the noise emitted by a scaled simplified nose landing gear following the LAGooN geometry in an aeroacoustic open–jet wind tunnel. An additional scaling of the frequency axis using the Strouhal number corresponding to each velocity was evaluated, but it only worsened the agreement between the different spectra for both emission directions.

2. Flyover direction

This section compares the noise emissions of the NLG in the flyover direction. Figure 20a presents the A–weighted sound pressure levels ($L_{\mathrm{p,A}}$) of the integrated narrow–band frequency spectra (corrected for the velocity influence taking $V_{\mathrm{ref}} = 65$ m/s) of an example flyover of each aircraft type, as well as the spectrum for the ALLEGRA model in the wind tunnel at $V = 65\,\mathrm{m/s}$. The spectrum of the ALLEGRA wind–tunnel model has been corrected to express the same frequency resolution as the flyover measurements ($\Delta f \approx 20$ Hz). Similar trends are observed between

the wind–tunnel and the flyover results. Unfortunately, the portion of the spectrum in common for both approaches is limited (1 kHz to 4 kHz). A good agreement is found between the wind–tunnel results and the flyover measurements for most of the 3–kHz–wide frequency interval, with noticeable differences only arising between 1000 Hz and 1400 Hz. Other flyover measurements of these aircraft types were similar to the ones presented here, but are not included for the sake of simplicity. Since the aircraft velocities are of the same order for the four cases shown in Fig. 20a, as well as the NLG geometries, differences in the Reynolds number are expected to be negligible. Potential causes for the differences between the wind–tunnel results and the flyover measurements could be differences in the NLG geometry and in the flow conditions, uncertainties when calculating the aircraft trajectory parameters (velocity, orientation, altitude, etc.), different installation effects of the NLG, and different propagation conditions from source to observer (atmospheric turbulence). [27]. Figure 20b presents the zoomed–in version of Fig. 20a.

It can be noticed that strong tonal noise is present for the three aircraft types at approximately 2200 Hz. This is especially the case for Aircraft Type C, for which a tone, protruding more than 12 dB higher over the broadband noise around it, is found. This phenomenon was already observed for other full–scale aircraft types by Michel and Qiao [12], by Dedoussi *et al.* [16] and by Merino–Martínez *et al.* [23, 30] and for wind–tunnel experiments featuring scale [4] or full–scale landing gears [15]. In some of these publications, it was suggested that the cause for these tonal peaks was the presence of open pin–cavities in the LG system. For the case of [15], it was determined that one of the main sources of tonal noise was the cavity of the pin that links the brakes and the brake–rods. The fact that no dependency was found in the current study between the tone frequency and the aircraft velocity (unlike with Aeolian tones) confirms the likelihood that these tones originate from a cavity [12, 16]. In addition, the expected vortex shedding frequency for the main strut of the NLG (with an approximate strut diameter d_{strut} of 0.1 m for all NLG geometries) considering the relation that the Aeolian tones typically occur for $St = f d_{\text{strut}}/V \approx 0.2$ [83] is approximately 140 Hz for $V = 70$ m/s, which is considerably lower than the frequency of the tones identified.

The theory of Rossiter [84] predicts the Strouhal number corresponding to the tone frequency $St = f_{\text{tone}}\, l_{cavity}/V$, based on the length of the cavity l_{cavity} and the true airspeed V, for different

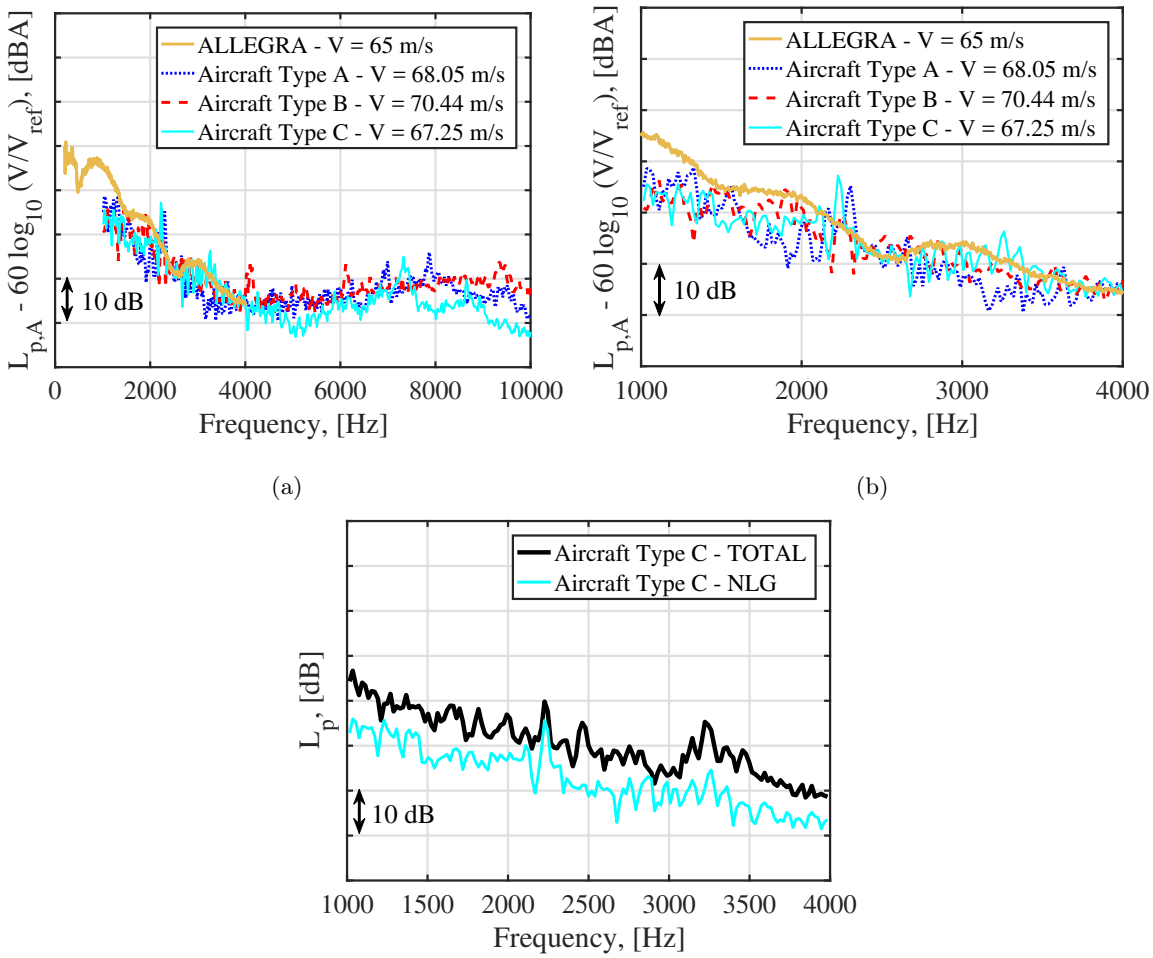

Fig. 20: (a) NLG spectra for a flyover of each aircraft type and the ALLEGRA wind–tunnel model. (b) Zoomed–in version of subfigure (a). (c) NLG and total aircraft spectra for an Aircraft Type C flyover.

Mach numbers. For a Mach number of around 0.2 like in this experiment, the expected Strouhal number for the cavity tonal noise is approximately 0.4. This would provide an approximate cavity length l_{cavity} of 13 mm. Since the geometries of the NLG for the three aircraft are similar, it is possible that they have cavities of similar dimensions as well, generating tones with comparable wavelengths. In addition, previous flyover measurements featuring larger NLG geometries [23, 40] presented tonal noise at lower frequencies (approximately 1700 Hz) and hence, larger wavelengths. The ratio between the wavelengths of the tonal noise of the experiment in [23] and the one of the present study agrees with the ratio between the axle lengths, providing more evidence that the

tonal noise is likely due to a cavity. On the other hand, no significant tones were present in the ALLEGRA model in this frequency range, most likely because it was designed to minimize pin hole and other related cavity tones based on such results to be found in the literature.

For the measured flyovers, the aforementioned tones were also present in the overall spectra of the whole aircraft, indicating the importance of NLG noise at around 2200 Hz. This is illustrated in Fig. 20c for the same flyover measurement of an Aircraft Type C as in Fig. 20a, where the NLG spectrum is compared to the total aircraft sound spectrum obtained using a single microphone and correcting for the propagation effects [51]. The tone at 2200 Hz is also present in the total aircraft spectrum. Removing the tone at that frequency would cause overall L_{p} reductions up to 1 dB (up to 2 dB if A–weighting is considered) for the frequency range considered. In addition, tonality is of high importance when assessing aircraft noise around airports, since it has been shown that tonal noise causes significantly more annoyance than broadband noise with the same $L_{\mathrm{p,A}}$ [40, 85, 86].

The far–field acoustic spectra obtained by the *Flyover array* in the computational simulations are presented in Fig. 21, where the Direct Numerical Beamforming (DNB) results using dual–LPD are shown, as well as the propagated signal using the FW–H analogy. The observer for the FW–H analogy is located at (x, y, z) = (2.826 m, 0 m, 3 m). The three different lines for DNB refer to how the deconvolution approach is performed: from below (DNB_b), from above (DNB_a) or in the optimal way (DNB_o). All the three approaches provided very similar results. Refer to [33] for further explanations. The vertical dashed line represents the limit of 5 kHz for good sound propagation due to the mesh resolution [33].

It can be observed that the three DNB approaches present a strong tonal peak (protruding about 20 dB over the surrounding broadband noise) approximately at 2100 Hz, which agrees with the tonal peaks found in the flyover measurements displayed in Fig. 20. The FW–H results, however, only present a tonal peak at about 1050 Hz, which is coincidentally half of the tonal frequency for DNB. The reason for this difference remains unknown and is subject for future research.

Figure 22a presents the comparison between the one–third–octave band spectra of the NLG emissions of three aircraft types, the ALLEGRA NLG from the wind–tunnel experiments (as presented in Fig. 20a) and the estimations of the three noise prediction models considered (Fink, Guo,

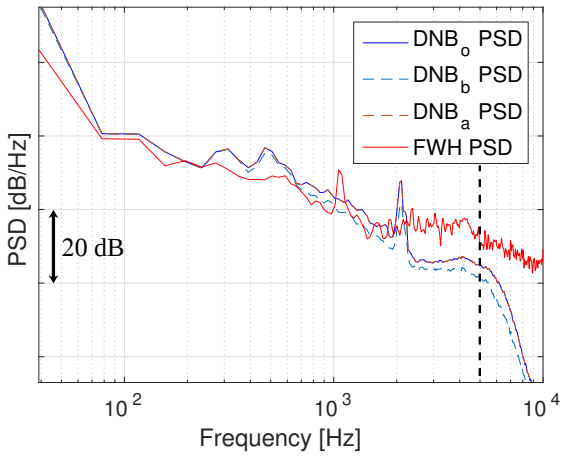

Fig. 21: Far–field acoustic spectra obtained by the *Flyover array* in the computational simulations with DNB and the FW–H analogy. Adapted from [33].

and DLR) using the geometry inputs of the ALLEGRA NLG model and a flow velocity $V = 65\,\mathrm{m/s}$. A first observation in the frequency range of common comparison (1 kHz to 4 kHz) indicates that Guo's model offers a better fit with the experimental data (especially with the flyover measurements) and that Fink's model tends to overpredict the noise emissions in this case by several dB. The method by DLR, on the other hand, seems to provide a close agreement with the spectrum of the ALLEGRA wind–tunnel model between 500 Hz and 1 kHz, but it considerably overestimates all the spectra for frequencies higher than that. Neither of the three noise prediction models seem to include the tonal peak at around 2 kHz (as expected), but they also do not consider the noise increase at higher frequencies (after 5 kHz). This high–frequency hump could be due to the aforementioned higher influence of the flow velocity in the noise levels at that frequency range (scaling with V^6 instead of V^7), due to the presence of small features of the NLG, see Fig. 19, that is not accounted in the prediction models. However, frequencies higher than 5 kHz have a smaller impact in aircraft community noise, since for typical distances between aircraft and noise sensitive areas, these frequencies are heavily attenuated due to the atmospheric absorption [21]. The wind–tunnel results present a *hump* between 500 Hz and 1600 Hz that is not captured by the noise prediction models either. The cause of this hump remains unknown, but the acoustic source plots show that the NLG is clearly the strongest noise source for every frequency in that range. Moreover, the

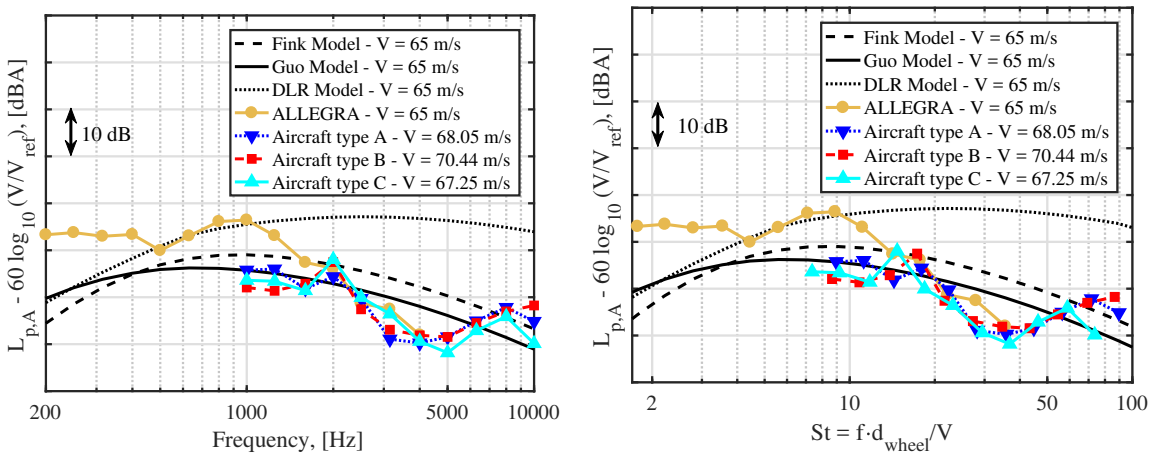

(a) (b)

Fig. 22: Comparison of the NLG noise emissions in the flyover direction ($\theta \approx 90°$, $\phi = 0°$): (a) Absolute frequencies. (b) Strouhal number ($St = f\, d_{\text{wheel}}/V$).

relatively high noise levels at low frequencies observed for the ALLEGRA NLG could be explained by the higher background noise levels at the wind–tunnel facility (including the presence of the bluff body of the fuselage belly) at that frequency range.

The integrated noise values in the frequency range between 1 kHz to 4 kHz predicted by Guo are considerably closer to those measured in the flyover experiments (within approximately a 1 dBA difference), whereas the predictions by Fink are approximately 4 dBA higher than the flyover experiments and those of the DLR method about 14 dBA higher.

Figure 22b depicts the same results as Fig. 22a but using the normalized frequency axis with the Strouhal number based on the wheel diameter ($St = f\, d_{\text{wheel}}/V$). In this case, the broadband frequency components above $St > 20$ of the three aircraft types seem to collapse better, but the tonal peaks are now slightly more spread within different Strouhal numbers.

3. Side direction

The integrated frequency spectra in the side direction for each of the ROIs defined in Figs. 12 and 13, namely the wheel and the strut and bay door of the ALLEGRA NLG, respectively, are presented in Fig. 23a, as well as the total NLG emissions. The spectrum of the ALLEGRA NLG

in the flyover direction from Fig. 22a is also displayed for reference. It can be observed that the noise contribution of the strut and bay door is slightly higher than that from the wheel, except for the one–third–octave band centered at 630 Hz, where the wheel presents considerably higher levels. Interestingly, the noise levels in the flyover direction are considerably lower than in the side direction for the whole frequency range, except between 800 Hz and 1200 Hz, where the aforementioned *hump* in the previous section causes an increase in the noise levels, even over the noise emissions in the side direction.

Figure 23b presents the comparison of the total noise emissions of the ALLEGRA NLG in the wind–tunnel tests in the side direction and the predictions of Fink's and Guo's models with $\phi = 90°$. The predictions of DLR's model, which considers the NLG as an omnidirectional sound source (i.e., same spectrum as in Fig. 22a), are also included. Once again, the wind–tunnel data present higher noise levels at low frequencies (below 400 Hz), which could be due to the higher background noise levels in the facility in that range. For frequencies higher than 400 Hz, the experimental data is bounded between the predictions of Fink's and Guo's noise prediction models, with a closer agreement to the results of Fink's model in this case. The predictions of the method by DLR seem to deviate from the experimental results, which could be explained by the lack of directivity assumed by the model. For this emission direction, the wind–tunnel data show another hump (smaller than for the flyover direction) between 1 kHz and 2.5 kHz. None of the noise prediction models capture this trend.

The far–field acoustic spectra obtained by the *Side array 2* in the computational simulations are presented in Fig. 24, which shows the DNB results using the three dual–LPD approaches aforementioned and the propagated signal using the FW–H analogy. In this case, only the DNB_a spectrum shows a small peak at 2100 Hz (protruding about 5 dB over the broadband noise), whereas the other two DNB spectra present no important tonal peaks in the whole frequency range. The FW–H results for an observer located at $(x, y, z) = (2.826\ \mathrm{m},\ 2\ \mathrm{m},\ 1.8\ \mathrm{m})$ contain several tonal peaks at about 1050 Hz and higher frequencies up to 2500 Hz. These peaks are not observed in the experimental data from the ALLEGRA wind–tunnel campaign.

Observing the source plots presented in Figs. 11 and 15, it could be proposed that the emissions

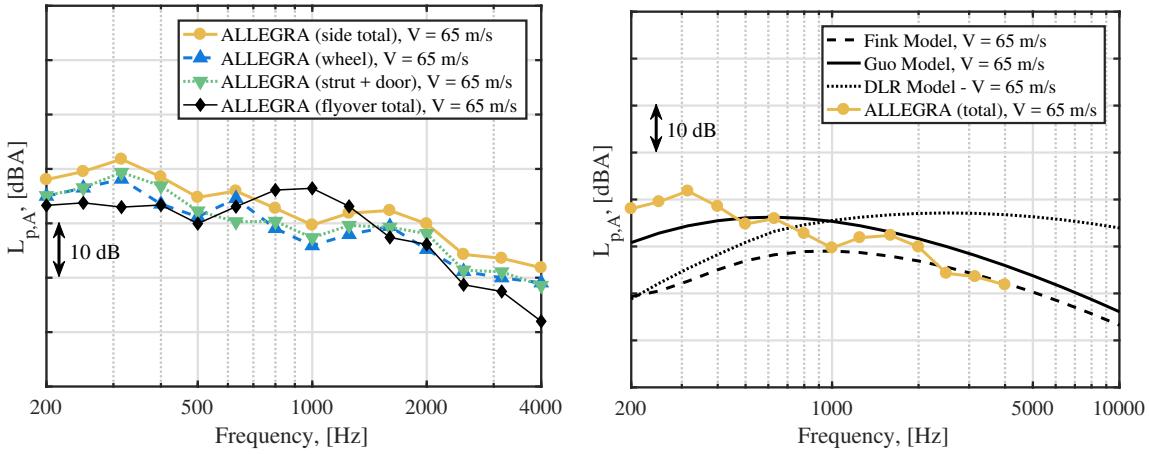

Fig. 23: Noise emissions of the NLG in the side direction ($\theta \approx 90°$, $\phi \approx 90°$): (a) Source breakdown. (b) Comparison with both noise prediction models.

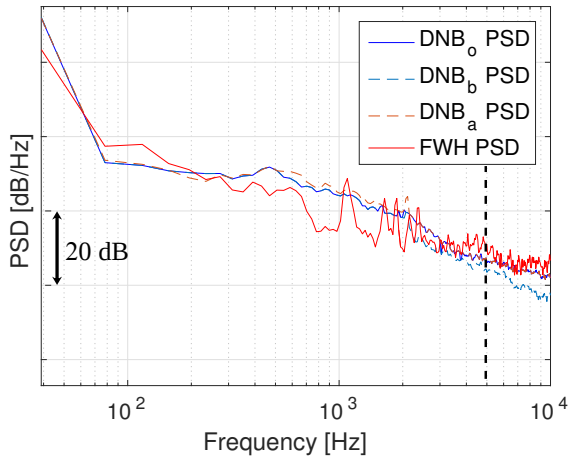

Fig. 24: Far–field acoustic spectra obtained by the *Side array 2* in the computational simulations with DNB and the FW–H analogy. Adapted from [33].

of the main noise sources found between the NLG wheels, and around the axle, are perhaps shielded by the presence of the wheels themselves, which would explain the lack of tonal peaks in the spectra presented in Fig. 24. Once again, a more detailed numerical analysis is suggested.

VI. Conclusions

This paper compares: 1) microphone–array measurements on full–scale nose landing gears (NLG) for regional aircraft performed in flyover tests for three aircraft types under operational conditions, 2) open–jet wind–tunnel experiments and 3) computational simulations. All the NLG have similar geometries. Different emission directions were studied, but the flyover and side directions are analyzed in detail. The application of acoustic imaging methods to the wind–tunnel and simulated microphone–array data allows for the estimation of the position and strength of the noise sources on the NLG. For the frequencies considered, the wind–tunnel tests and the computational simulations indicate that the main noise sources are located around the center of the wheel axle, followed by the main strut and bay doors.

The far–field sound spectra obtained from the wind–tunnel experiments follow the expected 6^{th} power law with the flow velocity. In addition, the wind–tunnel results show similar trends as those obtained for the flyover measurements, with the exception that the flyover results present strong tonal peaks around 2200 Hz, which are not observed in the wind–tunnel data. Such tones are considered to be of high annoyance for the population living near airports [40]. Removing these tones would cause overall noise reductions up to 2 dB in the frequency range examined. Similar tonal peaks at similar frequencies are also found in the outcome of the computational simulations. As proposed by previous research [5], it is suggested that these tones are caused by the presence of open cavities in the NLG system, since they do not seem to depend on the flow velocity. No important tonal peaks were observed in the side emission direction.

The obtained experimental results are compared with three widely–used airframe noise prediction models: Fink's, Guo's, and DLR's methods. The predictions of the first two methods present comparable trends with the experimental results, but do not consider the contributions of parasitic noise sources, such as cavities, in the calculations. Guo's method provides a closer agreement in the flyover emission direction, whereas Fink's method seems to offer a better match in the side emission direction.

Including cavity–noise estimations in the models would improve the noise predictions around airports [87]. However, cavity noise is considerably difficult to predict since the intensity of the

excitation of the cavity resonant mode depends on the velocity, turbulence levels and direction of the flow [84]. Moreover, the tones due to cavity noise must be considered individually and cannot be represented in a convenient nondimensional form [4]. The use of cavity caps might be an effective noise–reduction treatment [15] (keeping in mind practicality and safety constraints). Other noise–reduction devices [8–10, 28, 88, 89] can also help to reduce the LG emissions. In addition, due to the strong dependence between the noise emissions of the NLG (and most airframe noise sources, in general) and the flow velocity, an obvious recommendation would be to reduce the approach speed as much as possible, keeping in mind that the high–lift devices would generate more noise due to the additional lift requirement.

In conclusion, the importance of the use of phased microphone arrays in aeroacoustic experiments and simulations has been confirmed, as well as the advantages and limitations of different approaches in aeroacoustic studies. Overall, hybrid studies as the one presented in this paper are of high interest because they provide different insights that are not obtainable using a single approach and can help to fully understand the noise generation in landing gears. In the case presented here, flyover measurements showed the presence of strong tonal noise that was not measured in the wind–tunnel experiments. On the other hand, wind–tunnel tests allowed for a detailed study of the noise emissions and their scaling at different flow velocities and, together with the computational simulations, the location of the noise sources within the NLG system, which cannot be accurately determined in flyover measurements due to the relatively high distance between source and observer. Computational simulations even allow for emission angles that are not practical in other approaches, such as the upwind direction. In general, the use of these three approaches should be combined in order to update and improve the current noise prediction models, that seem to be too simple for detailed studies as this one. Future work is recommended, especially with dedicated setups that allow for a comparison over a larger frequency range than in the current study.

Acknowledgments

The research leading to the ALLEGRA wind–tunnel results has received funding from the European Union's Seventh Framework Programme (FP7/2007–2013) for the Clean Sky Joint Technology Initiative under grant agreements n° [308225] (ALLEGRA) and n° [620188] (ARTIC). Authors ac-

knowledge all the partners that took part in the ALLEGRA and ARTIC projects.

The authors also acknowledge Hamza Bouchouireb from the Royal Institute of Technology (KTH) in Stockholm, Sweden, for his constructive discussions about the computational results.

[1] "Environmental Noise Guidelines for the European Region," Tech. rep., World Health Organization. Regional Office for Europe, Copenhagen, Denmark, 2018.

[2] Ruijgrok, G., *Elements of aviation acoustics*, VSSD, Second ed., 2007, ISBN: 1090–6562–155–5.

[3] Lighthill, M. J., "On sound generated aerodynamically, I: General theory," *Proceedings of the Royal Society of London. Series A, Mathematical and Physical Sciences*, Vol. 211, No. 1107, 1952, pp. 564–587.

[4] Heller, H. H. and Dobrzynski, W. M., "Sound Radiation from Aircraft Wheel–Well/Landing–Gear Configuration," *Journal of Aircraft*, Vol. 14, No. 8, 1977, pp. 768–774.

[5] Dobrzynski, W., "Almost 40 Years of Airframe Noise Research: What Did We Achieve?" *Journal of Aircraft*, Vol. 47, No. 2, March–April 2010, pp. 353–367.

[6] "ACARE – Strategic Research & Innovation Agenda," Tech. rep., 2012.

[7] "Flightpath 2050 Europe's Vision for Aviation," Tech. rep., European Commission, 2012, ISBN: 978–92–79–19724–6.

[8] Neri, E., Kennedy, J., and Bennett, G., "Characterization of low noise technologies applied to a full scale fuselage mounted nose landing gear," *Proceedings of the Internoise 2015/ASME NCAD Meeting, August 9 – 12 2015, San Francisco, CA, USA*, 2015, NCAD2015–5911.

[9] Neri, E., Kennedy, J., and Bennett, G., "Aeroacoustic source separation on a full scale nose landing gear featuring combinations of low noise technologies," *Proceedings of the Internoise 2015/ASME NCAD Meeting, August 9 – 12 2015, San Francisco, CA, USA*, 2015, NCAD2015–5912.

[10] Kennedy, J., Neri, E., and Bennett, G., "The reduction of main landing gear noise," 22^{nd} *AIAA/CEAS Aeroacoustics Conference, May 30 – June 1 2015, Lyon, France*, 2016, AIAA paper 2016–2900.

[11] Green Regional Aircraft (GRA), "https://www.cleansky.eu/green-regional-aircraft-gra," Accessed in November 2019.

[12] Michel, U. and Qiao, W., "Directivity of Landing–Gear Noise Based on Flyover Measurements," 5^{th} *AIAA/CEAS Aeroacoustics Conference, May 10 – 12 1999, Bellevue, Greater Seattle, WA, USA*, 1999, AIAA paper 1999–1956.

[13] De Metz, F. C. and Farabee, T. M., "Laminar and Turbulent Shear Flow Induced Cavity Resonances," 4^{th} *AIAA Aeroacoustics Conference, October 3 – 5 1977, Atlanta, Georgia, USA*, 1977, AIAA paper 1977–1293.

[14] Elder, S. A., Farabee, T. M., and De Metz, F. C., "Mechanisms of flow–excited cavity tones at low Mach number," *Journal of the Acoustical Society of America*, Vol. 72, No. 2, August 1982, pp. 532–549.

[15] Dobrzynski, W., Chow, L. C., Guion, P., and Shiells, D., "A European Study on Landing Gear Airframe Noise Sources," 6^{th} *AIAA/CEAS Aeroacoustics Conference, June 12 – 14 2000, Lahaina, HI, USA*, 2000, AIAA paper 2000–1971.

[16] Dedoussi, I., Hynes, T., and Siller, H., "Investigating landing gear noise using fly–over data: the case of a Boeing 747–400," 19^{th} *AIAA/CEAS Aeroacoustics Conference, May 27 – 29, 2013, Berlin, Germany*, 2013, AIAA paper 2013–2115.

[17] Khelil, S., Bardoux, P., Godard, J., Le Garrec, T., Kennedy, J., and Bennett, G. J., "Investigation of the Noise Emission of a Regional Aircraft Main Landing Gear Bay," 23^{rd} *AIAA/CEAS Aeroacoustics Conference, June 5 – 9 2017, Denver, Colorado, USA*, 2017, AIAA paper 2017–3012.

[18] Bennett, G. J., Stephens, D. B., and Rodriguez Verdugo, F., "Resonant mode characterisation of a cylindrical Helmholz cavity excited by a shear layer," *Journal of the Acoustical Society of America*, Vol. 141, No. 1, January 2017, pp. 7–18.

[19] Neri, E., Kennedy, J., and Bennett, G. J., "Bay cavity noise for full–scale nose landing gear: A comparison between experimental and numerical results," *Aerospace Science and Technology*, Vol. 72, 2018, pp. 278–291.

[20] Pott-Pollenske, M., Dobrzynski, W., Buchholz, H., Guérin, S., Saueressig, G., and Finke, U., "Airframe Noise Characteristics from Flyover Measurements and Predictions," 12^{th} *AIAA/CEAS Aeroacoustics Conference, May 8 – 10 2006, Cambridge, Massachusetts, USA*, 2006, AIAA paper 2006–2567.

[21] Bertsch, L., *Noise Prediction within Conceptual Aircraft Design*, Ph.D. thesis, DLR, 2013, DLR Forschungsbericht, ISRN DLR–FB–2013–20, ISSN 1434–8454.

[22] Fink, M. R., "Noise component method for airframe noise," 4^{th} *AIAA Aeroacoustics Conference, October 3 – 5 1977, Atlanta, Georgia, USA*, 1977, AIAA paper 1977–1271.

[23] Merino-Martinez, R., Bertsch, L., Snellen, M., and Simons, D. G., "Analysis of landing gear noise during approach," 22^{nd} *AIAA/CEAS Aeroacoustics Conference, May 30 – June 1 2016, Lyon, France*, 2016, AIAA paper 2016–2769.

[24] Merino-Martinez, R., Neri, E., Snellen, M., Kennedy, J., Simons, D. G., and Bennett, G. J., "Comparing flyover noise measurements to full–scale nose landing gear wind–tunnel experiments for regional aircraft," 23^{rd} *AIAA/CEAS Aeroacoustics Conference, June 5 – 9 2017, Denver, Colorado, USA*, 2017, AIAA paper 2017–3006.

[25] Vieira, A., Mehmood, U., Merino-Martinez, R., Snellen, M., and Simons, D. G., "Variability of sound

quality metrics for different aircraft types during landing and take–off," 25^{th} *AIAA/CEAS Aeroacoustics Conference, May 20 – 24 2019, Delft, The Netherlands*, 2019, AIAA paper 2019–2512.

[26] Dobrzynski, W. and Buchholz, H., "Full–scale noise testing on Airbus landing gears in the German Dutch Wind Tunnel," 3^{rd} *AIAA/CEAS Aeroacoustics Conference, May 12 – 14 1997, Atlanta, GA, USA*, 1997, AIAA paper 1997–1597.

[27] Stoker, R., Guo, Y., Streett, C., and Burnside, N., "Airframe noise source locations of a 777 aircraft in flight and comparisons with past model–scale tests," 9^{th} *AIAA/CEAS Aeroacoustics Conference, May 12 – 14 2003, Hilton Head, South California, USA*, 2003, AIAA paper 2003–3232.

[28] Bennett, G. J., Neri, E., and Kennedy, J., "Noise Characterization of a Full-Scale Nose Landing Gear," *Journal of Aircraft*, Vol. 55, No. 6, 2018, pp. 2476–2490.

[29] Takaishi, T., Ura, H., Nagai, K., Yokokawa, Y., Muruyama, M., Ito, Y., Sakai, R., Shoji, H., and Yamamoto, K., "Airframe noise measurements on JAXA Jet Flying Test Bed 'Hisho'using a phased microphone array," *International Journal of Aeroacoustics*, Vol. 16, No. 4–5, 2017, pp. 255–273, SAGE Publications Ltd. London, United Kingdom.

[30] Merino-Martinez, R., Snellen, M., and Simons, D. G., "Functional beamforming applied to imaging of flyover noise on landing aircraft," *Journal of Aircraft*, Vol. 53, No. 6, November–December 2016, pp. 1830–1843.

[31] Simons, D. G., Snellen, M., Merino-Martinez, R., and Malgoezar, A. M. N., "Noise breakdown of landing aircraft using a microphone array and an airframe noise model," 46^{th} *International Congress and Exposition of Noise Control Engineering, 27–30 August, 2017, Hong Kong*, 2017.

[32] Snellen, M., Merino-Martinez, R., and Simons, D. G., "Assessment of noise level variability on landing aircraft using a phased microphone array," *Journal of Aircraft*, Vol. 54, No. 6, 2017, pp. 2173–2183.

[33] Bouchouireb, H., Pignier, N. J., O'Reilly, C., Boij, S., and Dahan, J., "Identification of noise sources on a realistic landing gear using numerical phased array methods applied to computational data," 23^{rd} *AIAA/CEAS Aeroacoustics Conference, June 5 – 9 2017, Denver, Colorado, USA*, 2017, AIAA paper 2017–3019.

[34] Dahan, J. A., O'Reilly, C., and Efraimsson, G., "Numerical Investigation of a Realistic Nose Landing Gear," 20^{th} *AIAA/CEAS Aeroacoustics Conference, June 16 – 20 2014, Atlanta, GA, USA*, 2014, AIAA paper 2014–2077.

[35] Dahan, J., Futrzynski, R., O'Reilly, C., and Efraimsson, G., "Aero–acoustic source analysis of landing gear noise via dynamic mode decomposition," 21^{st} *International Congress on Sound and Vibration, July 13 – 17 2014, Beijing, China*, Vol. 2, 2014, pp. 1245–1252.

[36] Redonnet, S. and Bulté, J., "Landing Gear Noise Sources Identification through an Application of Array Methods to Experimental and Computational Data," 22^{nd} *AIAA/CEAS Aeroacoustics Conference, May 30 – June 1 2016, Lyon, France*, 2016, AIAA paper 2016–2844.

[37] Guo, Y., "A Semi–Empirical Model for Aircraft Landing Gear Noise Prediction," 12^{th} *AIAA/CEAS Aeroacoustics Conference, May 8 – 10 2006, Cambridge, Massachusetts, USA*, 2006, AIAA paper 2006–2627.

[38] Burley, C. L., Brooks, T. F., Humphreys Jr., W. M., and Rawls Jr., J. W., "ANOPP Landing Gear Noise Prediction Comparisons to Model–Scale Data," 13^{th} *AIAA/CEAS Aeroacoustics Conference (*28^{th} *AIAA Aeroacoustics Conference), May 21 – 23 2017, Rome, Italy*, 2007, AIAA paper 2007–3459.

[39] Merino-Martinez, R., Neri, E., Snellen, M., Kennedy, J., Simons, D. G., and Bennett, G. J., "Analysis of nose landing gear noise comparing numerical computations, prediction models and flyover and wind–tunnel measurements," 24^{th} *AIAA/CEAS Aeroacoustics Conference, June 25 – 29 2018, Atlanta, Georgia, USA*, 2018, AIAA paper 2018–3299.

[40] Merino-Martinez, R., Vieira, A., Snellen, M., and Simons, D. G., "Sound quality metrics applied to aircraft components under operational conditions using a microphone array," 25^{th} *AIAA/CEAS Aeroacoustics Conference, May 20 – 24 2019, Delft, The Netherlands*, 2019, AIAA paper 2019–2513.

[41] Guo, Y., "Empirical Prediction of Aircraft Landing Gear Noise," Tech. Rep. NASA TM–2005–213780, NASA, July 2005.

[42] Mueller, T., *Aeroacoustic Measurements*, Springer Science & Business Media, 2002, ISBN: 978–3–642–07514–8.

[43] Kennedy, J., Eret, P., Bennett, G., Sopranzetti, F., Chiarotti, P., Castellini, P., Finez, A., and Picard, C., "The application of advanced beamforming techniques for the noise characterization of installed counter rotating open rotor," 19^{th} *AIAA/CEAS Aeroacoustics Conference, May 27 – 29 2013, Berlin, Germany*, 2013, AIAA paper 2013–2093.

[44] Bennett, G. J., Kennedy, J., Eret, P., Cappadona, F., Bianco, A., Letizia, R., Danise, D., Lamotte, L., Picard, C., Finez, A., Castellini, P., Chiarotti, P., Sopranzetti, F., Tsahalis, D., Tsahalis, H., Moussas, V., Paonessa, A., Amoroso, F., and Di Giulio, M., "WENEMOR: Wind Tunnel Tests for the Evaluation of the Installation Effects of Noise Emissions of an Open Rotor Advanced Regional Aircraft," 19^{th} *AIAA/CEAS Aeroacoustics Conference, May 27 – 29, 2013, Berlin, Germany*, 2013, AIAA paper 2013–2092.

[45] Merino-Martinez, R., Snellen, M., and Simons, D. G., "Functional Beamforming Applied to Full Scale Landing Aircraft," 6^{th} *Berlin Beamforming Conference, February 29 – March 1 2016, Berlin, Germany*,

GFaI, e.V., Berlin, 2016, BeBeC–2016–D12.

[46] Merino-Martinez, R., Snellen, M., and Simons, D. G., "Determination of Aircraft Noise Variability Using an Acoustic Camera," 23^{rd} *International Congress on Sound and Vibration, July 10 – 14 2016, Athens, Greece*, International Inst. of Acoustics and Vibration (IIAV), Auburn, Alabama, USA., July 2016.

[47] Merino-Martinez, R., Sijtsma, P., Snellen, M., Ahlefeldt, T., Antoni, J., Bahr, C. J., Blacodon, D., Ernst, D., Finez, A., Funke, S., Geyer, T. F., Haxter, S., Herold, G., Huang, X., Humphreys, W. M., Leclère, Q., Malgoezar, A., Michel, U., Padois, T., Pereira, A., Picard, C., Sarradj, E., Siller, H., Simons, D. G., and Spehr, C., "A review of acoustic imaging methods using phased microphone arrays (part of the Aircraft Noise Generation and Assessment special issue)," *CEAS Aeronautical Journal*, Vol. 10, No. 1, March 2019, pp. 197–230, DOI: 10.1007/s13272-019-00383-4.

[48] Lockard, D. P., Humphreys, W. M., Khorrami, M. R., Fares, E., Casalino, D., and Ravetta, P. A., "Comparison of Computational and Experimental Microphone Array Results for an 18%–Scale Aircraft Model," *International Journal of Aeroacoustics*, Vol. 16, No. 4–5, 2017, pp. 358–381, SAGE Publications Ltd. London, United Kingdom.

[49] Neri, E., *Characterisation and Reduction of Aircraft Landing Gear Noise*, Ph.D. thesis, Trinity College Dublin, 2017.

[50] Welch, P. D., "The Use of Fast Fourier Transform for the Estimation of Power Spectra: A Method Based on Time Averaging Over Short, Modified Periodograms," *IEEE Transactions on Audio and Electroacoustics*, Vol. AU–15, No. 2, June 1967, pp. 70–73.

[51] Snellen, M., Merino-Martinez, R., and Simons, D. G., "Assessment of aircraft noise sources variability using an acoustic camera," 5^{th} *CEAS Air & Space Conference, Challenges in European Aerospace, September 7 – 11 2015, Delft, Netherlands*, No. 2015–019, Council of European Aerospace Societies, September 2015.

[52] Howell, G. P., Bradley, M. A., McCormick, M. A., and Brown, J. D., "De–Dopplerization and acoustic imaging of aircraft flyover noise measurements," *Journal of Sound and Vibration*, Vol. 105, No. 1, Feb 1986, pp. 151–167.

[53] Sijtsma, P., "Phased array beamforming applied to wind tunnel and fly–over tests," Tech. Rep. NLR–TP–2010–549, National Aerospace Laboratory (NLR), Anthony Fokkerweg 2, 1059 CM Amsterdam, P.O. Box 90502, 1006 BM Amsterdam, The Netherlands, December 2010.

[54] Rossing, T. D., *Handbook of Acoustics*, Springer Science & Business Media, Second ed., 2007, ISBN: 987–0–387–30446–5.

[55] Shur, M. L., Spalart, P. R., Strelets, M. K., and Travin, A. K., "A hybrid RANS–LES approach with delayed–DES and wall–modelled LES capabilities," *International Journal of Heat and Fluid Flow*, Vol. 29, No. 6, 2008, pp. 1638–1649.

[56] Pignier, N. J., O'Reilly, C., and Boij, S., "Identifying equivalent sound sources from aeroacoustic simulations using a numerical phased array," *Journal of Sound and Vibration*, Vol. 394, No. Supplement C, 2017, pp. 203–219.

[57] Ffowcs Williams, J. E. and Hawkings, D. L., "Sound generation by turbulence and surfaces in arbitrary motion," *Philosophical Transactions of the Royal Society of London A – Mathematical, Physical and Engineering Sciences*, Vol. 264, No. 1151, May 1969.

[58] Amiet, R. K., "Refraction of sound by a shear layer," *Journal of Sound and Vibration*, Vol. 58, No. 4, 1978, pp. 467–482.

[59] Merino-Martinez, R., Sijtsma, P., and Snellen, M., "Inverse Integration Method for Distributed Sound Sources," 7^{th} *Berlin Beamforming Conference, March 5 – 6 2018, Berlin, Germany*, GFaI, e.V., Berlin, 2018, BeBeC–2018–S07.

[60] Merino-Martinez, R., Sijtsma, P., Rubio Carpio, A., Zamponi, R., Luesutthiviboon, S., Malgoezar, A. M. N., Snellen, M., Schram, C., and Simons, D. G., "Integration methods for distributed sound sources," *International Journal of Aeroacoustics*, Vol. 18, No. 4–5, 2019, pp. 444–469.

[61] Arce León, C., Merino-Martinez, R., Ragni, D., Avallone, F., and Snellen, M., "Boundary layer characterization and acoustic measurements of flow–aligned trailing edge serrations," *Experiments in Fluids*, Vol. 57, No. 182, October 2016, pp. 1 – 22.

[62] Arce León, C., Merino-Martinez, R., Ragni, D., Avallone, F., Scarano, F., Pröbsting, S., Snellen, M., Simons, D. G., and Madsen, J., "Effect of trailing edge serration–flow misalignment on airfoil noise emission," *Journal of Sound and Vibration*, Vol. 405, May 2017, pp. 19 – 33.

[63] Arce León, C., Merino-Martinez, R., Pröbsting, S., Ragni, D., and Avallone, F., "Acoustic Emissions of Semi–Permeable Trailing Edge Serrations," *Acoustics Australia*, Vol. 46, No. 1, 2017, pp. 111–117.

[64] Merino-Martinez, R., van der Velden, W. C. P., Avallone, F., and Ragni, D., "Acoustic measurements of a DU96–W–180 airfoil with flow–misaligned serrations at a high Reynolds number in a closed–section wind tunnel," 7^{th} *International Meeting on Wind Turbine Noise, May 2 – 5 2017, Rotterdam, the Netherlands*, 2017.

[65] Sijtsma, P., Merino-Martinez, R., Malgoezar, A. M. N., and Snellen, M., "High–Resolution CLEAN–SC: Theory and Experimental Validation," *International Journal of Aeroacoustics*, Vol. 16, No. 4–5, 2017, pp. 274–298, SAGE Publications Ltd. London, United Kingdom.

[66] Sijtsma, P., Merino-Martinez, R., Malgoezar, A. M. N., and Snellen, M., "High–Resolution CLEAN–SC: Theory and Experimental Validation," 23^{rd} *AIAA/CEAS Aeroacoustics Conference, June 5 – 9 2017, Denver, Colorado, USA*, 2017, AIAA paper 2017–3841.

[67] Luesutthiviboon, S., Malgoezar, A. M. N., Merino-Martinez, R., Snellen, M., Sijtsma, P., and Simons, D. G., "Enhanced HR–CLEAN–SC for resolving multiple closely spaced sound sources," *International Journal of Aeroacoustics*, Vol. 18, No. 4–5, 2019, pp. 392–413.

[68] Merino-Martinez, R., Luesutthiviboon, S., Zamponi, R., Rubio Carpio, A., Ragni, D., Sijtsma, P., Snellen, M., and Schram, C., "Assessment of the accuracy of microphone array methods for aeroacoustic measurements," *Journal of Sound and Vibration*, 2019, Accepted for publication.

[69] Dougherty, R. P., "Functional Beamforming," 5^{th} *Berlin Beamforming Conference, February 19 – 20 2014, Berlin, Germany*, GFaI, e.V., Berlin, 2014.

[70] Dougherty, R. P., "Functional Beamforming for Aeroacoustic Source Distributions," 20^{th} *AIAA/CEAS Aeroacoustics Conference, June 16 – 20 2014, Atlanta GA, USA*, 2014, AIAA paper 2014–3066.

[71] Camier, C., Padois, T., Provencher, J., Gauthier, P.-A., Berry, A., Blais, J. F., Patenaude-Dufour, M., and Lapointe, R., "Fly–over source localization on civil aircraft," 19^{th} *AIAA/CEAS Aeroacoustics Conference. May 27 – 29 2013. Berlin, Germany*, 2013, AIAA paper 2013–2261.

[72] Dougherty, R. P., "Cross Spectral Matrix Diagonal Optimization," 6^{th} *Berlin Beamforming Conference, February 29 – March 1, 2016, Berlin, Germany*, GFaI, e.V., Berlin, 2016.

[73] Dougherty, R. P., Ramachandran, R. C., and Raman, G., "Deconvolution of Sources in Aeroacoustic Images from Phased Microphone Arrays Using Linear Programming," 19^{th} *AIAA/CEAS Aeroacoustics Conference, May 27 – 29 2013, Berlin, Germany*, 2013, AIAA paper 2013–2210.

[74] Brooks, T. F. and Humphreys, W. M., "A Deconvolution Approach for the Mapping of Acoustic Sources (DAMAS) determined from phased microphone arrays," *Journal of Sound and Vibration*, Vol. 294, No. 4-5, 2006, pp. 856–879.

[75] Zorumski, W. E., "Aircraft Noise Prediction Program – Theoretical Manual – Part 1," Tech. Rep. NASA Technical Memorandum 83199, NASA Technical Memorandum 83199, 1982.

[76] Zorumski, W. E., "Aircraft Noise Prediction Program – Theoretical Manual – Part 2," Tech. Rep. NASA Technical Memorandum 83199, NASA Technical Memorandum 83199, 1982.

[77] Curle, N., "The influence of solid boundaries upon aerodynamic sound," *Proceedings of Royal Society of London A*, Vol. 231, No. 1187, September 1955, pp. 505–514.

[78] Bertsch, L., Dobrzynski, W., and Guérin, S., "Tool Development for Low–Noise Aircraft Design," *Journal of Aircraft*, Vol. 47, No. 2, March–April 2010, pp. 694–699.

[79] Bertsch, L., Guérin, S., Looye, G., and Pott-Pollenske, M., "The Parametric Aircraft Noise Module – status overview and recent applications," 17^{th} *AIAA/CEAS Aeroacoustics Conference (*32^{nd} *AIAA Aeroacoustics Conference), 5 – 8 June 2011, Portland, Oregon, USA*, 2011, AIAA paper 2011–2855.

[80] Merino-Martinez, R., *Microphone arrays for imaging of aerospace noise sources*, Ph.D. thesis, Delft University of Technology, 2018, ISBN: 978–94–028–1301–2.

[81] Guo, Y., Yamamoto, K. J., and Stoker, R. W., "Experimental Study on Aircraft Landing Gear Noise," *Journal of Aircraft*, Vol. 43, No. 2, November–December 2006, pp. 306–317.

[82] Liu, P., Xing, Y., Guo, H., and Li, L., "Design and performance of a small–scale aeroacoustic wind tunnel," *Applied Acoustics*, Vol. 116, 2017, pp. 65–69.

[83] Glegg, S. and Devenport, W. J., *Aeroacoustics of Low Mach Number Flows – Fundamentals, Analysis, and Measurement*, Academic Press, 2017, ISBN: 978–0–128–09651–2.

[84] Rossiter, J. E., "Wind Tunnel Experiments on the Flow Over Rectangular Cavities at Subsonic and Transonic Speeds," Tech. Rep. Technical Report No. 64037, Royal Aircraft Establishment, October 1967.

[85] Aures, W., "Procedure for calculating the sensory euphony of arbitrary sound signal," *Acustica*, Vol. 59, No. 2, 1985, pp. 130–141.

[86] Merino-Martinez, R., Pieren, R., Snellen, M., and Simons, D. G., "Assessment of the sound quality of wind turbine noise reduction measures," 26^{th} *International Congress on Sound and Vibration, July 7 – 11 2019, Montreal, Canada*, International Inst. of Acoustics and Vibration (IIAV), Auburn, Alabama, USA., July 2019.

[87] Pieren, R., Bertsch, L., Lauper, D., and Schäffer, B., "Improving future low–noise aircraft technologies using experimental perception–based evaluation of synthetic flyovers," *Science of the Total Environment*, Vol. 692, July 2019, pp. 68–81.

[88] Eret, P., Kennedy, J., and Bennett, G. J., "Effect of noise reducing components on nose landing gear stability for a mid–size aircraft coupled with vortex shedding and freeplay," *Journal of Sound and Vibration*, Vol. 354, October 2015, pp. 91–103.

[89] Zhao, K., Okolo, P., Neri, E., Chen, P., Kennedy, J., and Bennett, G. J., "Noise Reduction Technologies for Aircraft Landing Gear – A Bibliographic Review," *Progress in Aerospace Sciences*, 2019.